Applied Magnetic Resonance (2024) 55:889–922
https://doi.org/10.1007/s00723-024-01658-8

**Applied
Magnetic Resonance**

REVIEW

PELDOR to the Metal: Cu(II)-Based Labels Put a New Spin on Distance Measurements

Joshua Casto[1] · Shramana Palit[1] · Sunil Saxena[1]

Received: 15 March 2024 / Revised: 24 April 2024 / Accepted: 28 April 2024 /

Abstract

Eighty years ago, the advent of electron paramagnetic resonance (EPR) revolutionized our ability to observe the physical world of unpaired electron spins. The inception of EPR spawned multiple scientific areas with a focus on discerning the roles of paramagnetic metals and organic radicals in an array of processes and materials. More recently, the emergence of site-directed spin labeling combined with distance measurement technology and molecular modeling has harnessed the power of EPR, to 'watch proteins move'. Spin labels have enabled the measurement of distance constraints and site-specific dynamics in biomolecules to provide rich details of structure and structural changes that are tightly linked to biological function. Historically, nitroxide radicals are the most common spin labels. However, decades of method development and technological innovation have created a plethora of spin label types to extend the reach of EPR throughout the realm of biophysics. In this review we overview recent developments that improve the sensitivity of distance measurements using Cu(II) labels. These achievements over the last three years promise advancements in the ability of EPR to measure structural and dynamical constraints beyond what is possible using common spin labels. First, we briefly discuss pulsed and continuous-wave EPR techniques that discern the coordination of Cu(II) to monitor spin-labeling efficiency and binding in biological environments. Next, we outline the bottlenecks that impact sensitivity in pulsed dipolar spectroscopy and the strategic steps taken to remove these bottlenecks to collect distance measurements in hours. More precisely, we focus on the fast-spin phase memory relaxation time, the broad EPR spectrum due to anisotropy, and orientational selectivity effects inherent to Cu(II). Finally, we showcase the versatile application of Cu(II) spin labels in biological systems and the advantages of Cu(II) in pulsed dipolar spectroscopy to access nanomolar protein concentrations.

Extended author information available on the last page of the article

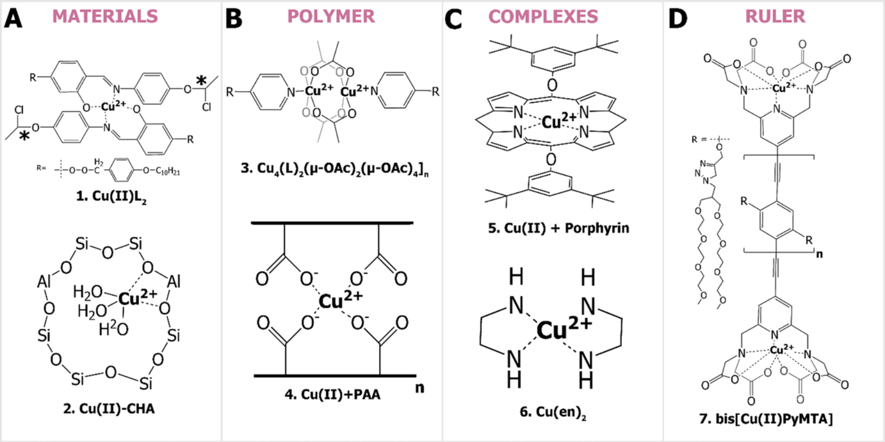

Fig. 1 Various Cu(II) systems, materials, and spin labels studied by EPR. **A** (1) optics Cu(II)L_2 and (2) zeolite Cu(II)-CHA. **B** polymers (3) monomeric unit $Cu_4(L)_2(\mu\text{-OAC})_2(\mu\text{-OAC})_4]_n$ and (4) monomeric unit of hydrogel Cu(II) + PAA (polyacetic acid). **C** complexes (5) Cu(II) porphyrin and (6) Cu(II) binding site in functionalized clay. **D** ruler (7) bis[Cu(II)PyMTA]

1 Introduction

Electron paramagnetic resonance (EPR) is an indispensable tool for understanding the role of free radicals and paramagnetic metals in many branches of science [1]. Continuous-wave (CW) and pulsed EPR measurements are commonly used to elucidate the coordination environment, probe electron–nuclear interactions, and measure the distance between two or more spin labels. The diversity of EPR methods has been pivotal to discern a variety of phenomena that ranges from radical propagation in biological processes, metal coordination in inorganic assemblies, and to the state of qubits in quantum computing. These applications span across various materials that contain stable organic radicals like nitroxides or paramagnetic metals such as Gd(III), Fe(II), Fe(III), Mn(II), and Cu(II). In this review, we focus on Cu(II)-based EPR applications given that Cu(II) has increasing relevance as an EPR probe across scientific disciplines.

1.1 Cu(II)-Based EPR in Materials

Figure 1 shows illustrative examples of Cu(II) probes and labels that have been used to determine structure–function relationships in materials, polymers, and functional complexess. For example, EPR has determined the molecular arrangement of Cu(II) coordination for the development of optical materials (Fig. 1A) [2] and tracked the activity of Cu(II) in a zeolite cage (Fig. 1A) [3]. EPR has also delineated the two Cu(II) coordination sites in a polymer (Fig. 1B) [4], characterized the Cu(II) dependent mechanical properties of hydrogels (Fig. 1B) [5], discerned the assembly and geometry of a Cu(II) mediated porphyrin (Fig. 1C) [6], and elucidated the mechanism of Cu(II) exchange with salts in functional clays (Fig. 1C) [7]. Additionally, synthesized molecules with two terminal Cu(II) sites are used as standard rulers for the development of distance measurement methodology (Fig. 1D) [8]. EPR is also commonly used to characterize the synthesis and function of Cu(II)-based metal organic frameworks [9–11]. In spintronics, Cu(II) dimer complexes are often used to investigate the transfer of spin quantum information over distances [12, 13].

1.2 Cu(II)-Based EPR in biology

EPR is especially advantageous for biophysical applications of structure and dynamics given that the measurements have no size limitations and can be performed in solution, in-cell, in membranes, or in membrane mimics [14–16]. Moreover, the specificity of EPR for unpaired electrons makes it only sensitive to the analyte in the presence of other biological compounds. The biophysical information that EPR provides is crucial in establishing the link between structure and function of biomolecules that govern biological processes.

Many classes of proteins bind Cu(II) natively. These Cu(II)-binding proteins have an exploitable endogenous EPR active site to probe dynamics, determine coordination environment, and measure distances. For example, EPR has routinely exploited native Cu(II) coordination in many proteins to gain pertinent structural insights (Fig. 2A) [17–23]. Figure 2 shows examples of native Cu(II) coordination in prion proteins and azurin.

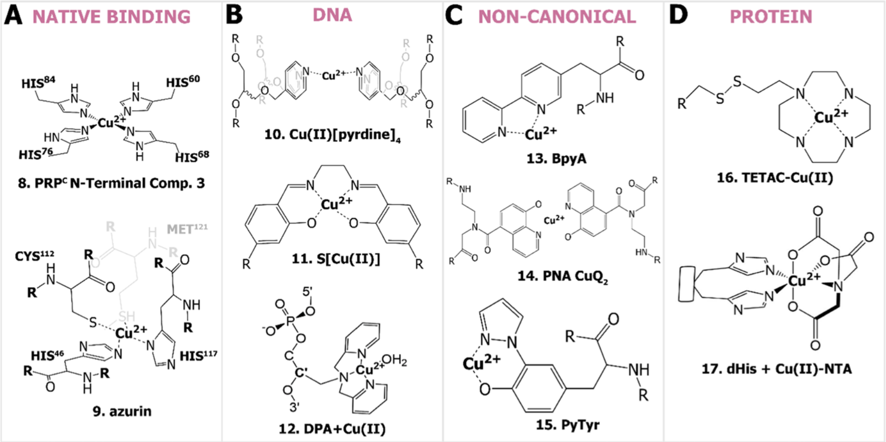

Fig. 2 Various Cu(II) systems for biological EPR applications **A** Cu(II) binding sites in (8) N-terminal component 3 of prion protein PRP^c and (9) azurin. **B** DNA labels (10) Cu(II)[pyridine]$_4$ in G-quadruplex DNA, (11) S[Cu(II)], and (12) DPA + Cu(II). **C** Spin labels introduced via non-canonical amino acids or residues (13) BpyA, (14) CuQ$_2$ in protein nucleic acid structure, (15) PyTyr. **D** Protein spin labels (16) TETAC–Cu(II) via cysteine linkage and (17) the rigid coordination of Cu(II)–NTA to the double histidine motif

On the other hand, for biomolecules that do not bind Cu(II) naturally, Cu(II) can be introduced into the biomolecule [24] via site-directed spin labeling [25, 26]. For instance, Cu(II) can be incorporated into DNA via chelator(s) (Fig. 2B) substituted in the place of a nucleobase [27–29]. There are also spin labels that use non-canonical residues that coordinate Cu(II) to label the protein [30, 31] or protein-nucleic acid (Fig. 2C) [32]. In addition, a Cu(II)-chelator moiety can be incorporated via disulfide linkage with cysteine (Fig. 2D) [33]. Moreover, the double histidine (dHis) motif is a straightforward spin labeling approach to specifically incorporate Cu(II) into a protein (Fig. 2D) [34].

1.3 The dHis Motif

The dHis motif enables a cysteine-free means to directly measure structural constraints [34] and site-specific dynamics in proteins [35]. The protein label strategically incorporates histidine residues at i, $i+4$ and i, $i+2$ positions in α-helices and β-sheets respectively. These residue separations engender specific chelation of a liganded Cu(II) complex [36, 37] for optimal spin-labeling efficiency without additional synthesis. The anchoring of the Cu(II) complex by dHis forms a small and rigid spin label that yields pulse dipolar spectroscopy (PDS) distance distributions [38] up to five times narrower than commercially available nitroxides [39]. In addition, force field parameters of the protein label have been developed to relate sparse EPR distance constraints to atomic level details with molecular dynamics (MD) simulations [32].

Even though Cu(II)-EPR is an incisive tool, attributes of this EPR probe can be non-intuitive. Therefore, we provide this review to conceptually overview the use of Cu(II)-EPR in many contexts. We briefly highlight the use of EPR to measure Cu(II)-coordination. The bulk of the review then focuses on more recent work on improving the sensitivity of pulsed dipolar spectroscopy of Cu(II)-spins. Here we review the attributes of Cu(II) that hinder sensitivity for distance measurements, and then discuss recent methodological advances in this arena. Finally, we highlight recent applications of Cu(II)-EPR for measurements of structure–functions relationships in proteins and nucleic acids. Moreover, even though this review focuses on Cu(II) probes, we refer the reader to in-depth reviews highlighting the biological application and sensitivity of nitroxide [40–42], Gd(III) [43, 44], and trityl [45–47] spin labels [46, 48, 49].

2 Cu(II) Coordination

Importantly, CW-EPR is often used to determine the coordination environment of Cu(II). In the context of Cu(II)-spin labeling, such experiments are also useful to ascertain labeling efficiency. The foundational work that establishes the use of CW-EPR to gain insight into Cu(II) coordination has been well established and reviewed [50–55]. Briefly, CW-EPR spectra provide g-tensors and hyperfine values (A) of Cu(II) that are sensitive to the geometry of coordination and the type of atoms directly coordinated to Cu(II). Figure 3A shows three complexes, in which the number of equatorially coordinated nitrogen (N) and oxygen (O) atoms are 4N (i and ii) and 2N2O (iii), respectively. These atoms are designated by a filled pink circle in Fig. 3A. The CW-EPR and electron spin-echo envelope modulation (ESEEM) features of these complexes have been systematically examined in previous work [56]. Figure 3A also shows the dHis-Cu(II) label which contains a 3N1O equatorial coordination. Such changes in coordination lead to changes in the g-tensors and hyperfine values [50].

Figure 3B shows CW-EPR spectra collected for the three Cu(II) complexes and compares the data with free Cu(II). The changes in spectral features with the changes in coordination environment are clear. The "splittings" due to $A_{||}$ are readily visible in the low-field regions of the spectrum. Their relative positionings are highlighted

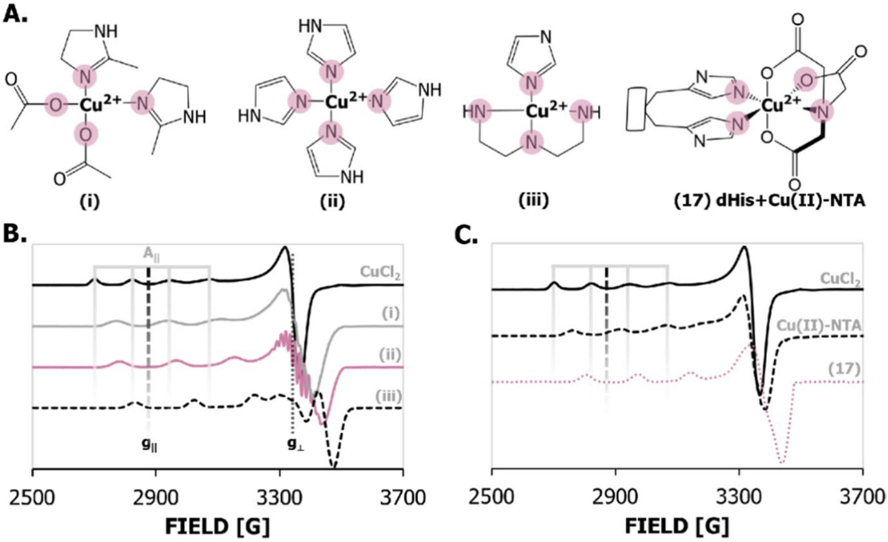

Fig. 3 **A** Structures of (i) bis(2-methylimidazole)copper(II) diacetate (two imidazole), (ii) tetrakisimidiazolecopper(II) sulphate (four imidazole), (iii) dienimidazolecopper(II) diperchlorate (one imidazole), and (17) dHis and copper(II) nitrilotriacetic acid (Cu(II)–NTA). Directly coordinated atoms are highlighted—nitrogen and oxygen (pink). **B** CW-EPR spectra of $CuCl_2$ to complexes (i), (ii), and (iii). The $g_{||}$ decreases and $A_{||}$ increases as the number of nitrogen atoms that are coordinated to Cu(II) increases. Such differences are easily observable by the shifts in the spectral peak positions. Grey bars are used as guides for the eyes to highlight the difference in peak separation as the combination of coordinated nitrogen and oxygen to Cu(II) changes. The simulations for the spectra are presented in the S.I. **C** CW-EPR spectra of $CuCl_2$, free Cu(II)–NTA, and the dHis Cu(II) protein label (17). Positionings of $g_{||}$ (grey dashed), $A_{||}$ (solid grey), and $g_{\perp}$ (black dashed) relative to $CuCl_2$ are shown. The $g_{||}$ and $A_{||}$ increase and decrease respectively as the number of nitrogen atoms coordinated to Cu(II) increases as depicted by the shifts in the spectral peak positions. The grey bars are used as guides to highlight the difference in line shapes. The Cu(II) imidazole complexes were prepared to (i) 4.6 mM, (ii) 6.6 mM, and (iii) 17 mM. The $CuCl_2$ was prepared to 400 μM and the dHis sample was prepared by adding 200 μM 15H/17H/28H/32H GB1 mutant with 400 μM of Cu(II)–NTA. Experiments were performed at 80 K over 1024 points using a 4 G modulation amplitude at an attenuation of 20 dB. Sample preparation and data collection were performed as originally described in Silva et al. [56]. Details of data collection, analysis, and synthesis of the Cu(II) complexes are provided in S.I. (Color figure online)

by grey lines for the $CuCl_2$ spectrum. These splittings change as the nature of the coordinating atom changes. Table 1 provides the $A_{||}$ and $g_{||}$ for all samples. Complex (i), with a 2N2O coordination has a higher $g_{||}$ and lower $A_{||}$ compared to (ii) and (iii), which have a 4N coordination.

The changes in the spectra occur because the oxygen molecules from water coordinated to Cu(II) in $CuCl_2$ are replaced with nitrogen atoms from varying numbers of imidazole in the complexes. The lower electronegativity of nitrogen compared to oxygen results in a more covalent bond to Cu(II). These differences in the covalency lead to changes in the spin orbit coupling in Cu(II), which causes changes in the g-tensor values [50, 58]. Similarly the increased electron density around Cu(II) with increasing nitrogen coordination increases Fermi contact [1]. Therefore, replacing the oxygen atoms coordinated to Cu(II) with nitrogen atoms increases the hyperfine interaction, $A_{||}$ [50]. In addition, complex (ii) and (iii) have 4N coordination but have slightly different $A_{||}$ and $g_{||}$ values. The basicity of the solution deprotonates the nitrogen of imidazole. Therefore since (iii) is coordinated to two more imidazole than (ii) the complexes have different overall net charges, which causes differences in the $A_{||}$ and $g_{||}$ values of these complexes, even though both have the Cu(II) directly coordinated to four nitrogen atoms [50].

Such CW-EPR data can, therefore, be useful to determine that Cu(II)–NTA is properly chelating to dHis. Figure 3C compares the CW-EPR data of $CuCl_2$, the free Cu(II)–NTA label and the label attached to a dHis site on protein GB1. The coordination of the label to protein results in a change in coordination compared to the free label in solution, which leads to distinct changes in the spectral lineshape. Table 1 reports the g and A tensors for these data. Note, however, that there is a range of values for these parameters in spin labeled proteins depending on the site of labeling [59] and the buffer [60].

In addition, pulsed-EPR experiments are often utilized to obtain a more comprehensive idea of the moiety that surrounds the spin center. The pulsed experiments ESEEM [61] and hyperfine sub-level correlation [62, 63] provide rich information

Table 1 CW-EPR lineshape g-tensor and hyperfine (A) values for Cu(II) complexes presented in Fig. 3. All values were obtained from EasySpin simulations

Sample	$g_{\perp}$[a]	$g_{\|\|}$[a]	$A_{\perp}$[a] [G]	$A_{\|\|}$[a] [G]
$CuCl_2$	2.076	2.415	12	121
Cu(II)–NTA	2.065	2.318	11	143
dHis + Cu(II)–NTA	2.058	2.275	5	166
(i)[b, c]	2.060	2.284	7	163
(ii)[b, c]	2.055	2.260	7	180
(iii)[b]	2.046	2.210	17	192

[a] Values were obtained via spectral fitting using EasySpin [57] 5.2.35 in MATLAB 2020b

[b] The complexes (i)–(iii) were prepared and the CW ESR data was collected and analyzed as previously described in Silva et al. [56]

[c] For complexes (i) and (ii) the superhyperfine splitting from coordinated nitrogen at 3300 G were not included in the simulations. Note that, $g_{||}$ and $A_{||}$ are of interest to determine Cu(II) coordination and these are well resolved

about the nuclear environment of Cu(II) [64, 65] to complement CW-EPR spectra. Both techniques are sensitive to the nuclear quadrupole interaction of nitrogen and hyperfine interactions between the spin center and remote nuclei in an approximate 0.3–0.8 nm radius [61]. Figure 4A shows remote nitrogen (dashed circles) in the Cu(II) complexes. The interaction between the Cu(II) electron spin and remote nitrogens (and protons) are easily detected by ESEEM. As such, ESEEM can also be a powerful technique to determine the number of histidine residues coordinated to Cu(II) [18, 56, 66–68]. Here, we provide ESEEM analysis of the imidazole Cu(II) complexes to illustrate Cu(II) coordination to dHis.

Figure 4B shows the ESEEM spectra for complexes (i)–(iii). Each complex contains a different number of imidazole ligands. These numbers are one for complex (iii), two for complex (i), and four for complex (ii). Note, that two imidazoles from

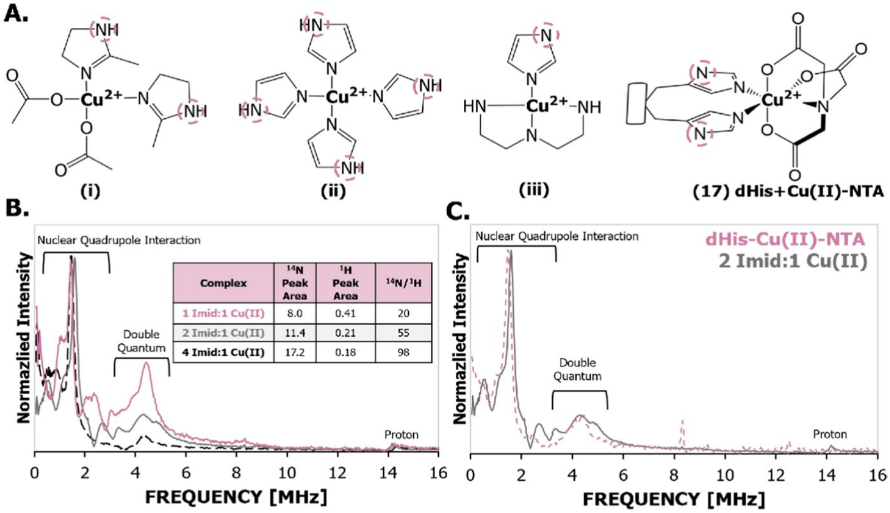

Complex	^{14}N Peak Area	^{1}H Peak Area	$^{14}N/^{1}H$
1 Imid:1 Cu(II)	8.0	0.41	20
2 Imid:1 Cu(II)	11.4	0.21	55
4 Imid:1 Cu(II)	17.2	0.18	98

Fig. 4. **A** Structures of (i) bis(2-methylimidazole)copper(II) diacetate (two imidazole), (ii) tetrakisimidiazolecopper(II) sulphate (four imidazole), (iii) dienimidazolecopper(II) diperchlorate (one imidazole), and the dHis and copper(II) nitrilotriacetic acid (Cu(II)–NTA) complex. Remote nitrogen that are detectable by ESEEM are circled. **B** ESEEM spectra of Cu(II)-imidazole complexes (i), (ii), and (iii) from Fig. 3A. The frequency peaks between 0–8 MHz are characteristic of interactions between Cu(II) and the remote nitrogen of the imidazole. Nuclear quadrupole interaction peaks appear between 0–2 MHz. The double quantum peaks appear at ~ 4 and 8 MHz, respectively. The peak at 14 MHz is characteristic of proton interactions. The pulses were separated to minimize, but not entirely remove, proton detection. The intensity of the double quantum peak increases in parallel with the number of imidazole coordinated to Cu(II). The table inset shows the ratio of the nitrogen to proton peak areas to quantify the increasing nitrogen interactions with imidazole coordination. **C** ESEEM spectra of the two imidazole Cu(II) complex (iii) and the 15H/17H/28H/32H mutant of GB1 labeled with Cu(II)–NTA. The peak positioning and intensities of the two spectra are in good agreement, indicating Cu(II)–NTA coordinates to two histidine residues. ESEEM was performed on imidazole Cu(II) complexes at concentration (i) 4.6 mM, (ii) 6.6 mM, (iii) 17 mM, and 200 μM of 15H/17H/28H/32H dHis GB1 loaded with 400 μM Cu(II)–NTA. The data was phased, fast Fourier transformed, and then normalized relative to the peak of greatest intensity. Experiments were performed at 18 K with a 3 dB attenuation. Data was collected and analyzed using the original method as previously described in Silva et al. [56]. Details of data collection, analysis, and synthesis of the Cu(II) complexes are provided in S.I

the two His sidechains coordinate to Cu(II)–NTA in the dHis motif (c.f. Figure 4A, complex 17). These remote nitrogens are designated by dashed circles in Fig. 4A. First, the interaction with the remote nitrogen leads to three peaks below 2 MHz, whose positioning depends on the nuclear quadrupolar interaction of nitrogen [69–72]. In addition, there is a peak around 4 MHz—this is referred to as the double quantum peak [64, 73, 74]. Second, as the quantity of imidazoles that are coordinated to Cu(II) increases, the double quantum peak at 4 MHz increases in intensity relative to the peaks below 2 MHz [56]. This effect is clearly seen in the ESEEM spectra from the three complexes in Fig. 4A.

In addition, when data are carefully collected under the same conditions the normalized intensity ratio of the nitrogen peaks (e.g., 0–8 MHz) to the proton peak (14 MHz) can quantify the number of remote nitrogens [56, 66, 67]. The table inset shows the increasing area of the nitrogen peaks relative to the proton peak at 14 MHz. The peaks were normalized, integrated, and weighted against the proton peak to show the increasing integrated intensity of nitrogen peaks monotonically with imidazole coordination.

The unique fingerprint ESEEM spectra of these imidazole complexes are useful to characterize the number of histidine coordinated to Cu(II) for biological applications [18, 66, 75, 76]. For example, Fig. 4B shows that the spectra of the two imidazole complex (i) and the dHis label are in good agreement. The agreement in spectra indicates Cu(II) binds to two histidine residues since both complexes have the same number of remote nitrogen (cf. Fig. 4A). However. even though these local nuclear interactions are useful to characterize Cu(II) binding, these nuclear interactions significantly affect the physical behavior of Cu(II) spins with respect to PDS sensitivity. These effects are discussed in the next section.

3 Sensitivity Considerations for PDS Using Cu(II)

Recently, the measurement of point-to-point distances in biomolecules using either endogenously bound Cu(II) or site-specifically labeled Cu(II) has emerged as a robust and versatile biophysical technique [34]. Work highlighting such applications will be outlined in detail later in this review. Given the robustness of this technique, there is considerable interest in enhancing the sensitivity of Cu(II)-based PDS distance measurements to expand the range of accessible biological applications, to accelerate data-collection times, and to make the technology itself more user friendly. Herein we outline the common sensitivity challenges of Cu(II) spins for PDS measurements and the respective strides in method development that have been used to ameliorate these sensitivity obstacles.

3.1 Relaxation Challenges

The spin relaxation time (T_1) and the phase memory time (T_m) of Cu(II) are critically important for the sensitivity of PDS signals. Generally, for PDS, T_1 determines the wait time between each measurement [77]. On the other hand, T_m impacts the intensity of the PDS signal. PDS measurements rely on the acquisition of an echo from two pulses [78–80], and the longer the distance the longer the pulse separation needed between these pulses. This idea is shown conceptually in Fig. 5 for the case of double electron–electron resonance (DEER) (also known as pulsed electron–electron double resonance, PELDOR) [81, 82]. For this experiment a long distance requires a longer value of τ_2. However, as τ_2 gets longer the echo intensity decreases which decreases the sensitivity [83].

Previous work has shown that geometry of Cu(II) coordination influences both T_1 and T_m times due to differences in nuclear interactions [84, 85]. Notably, tetrahedral and octahedral Cu(II) complexes tend to have faster relaxation rates compared to square planar structures, whether it be a small compound or coordinated in a protein [85]. At the usual Cu(II) measurement temperature of 20 K, T_1 is approximately 100–300 μs depending on the complex. As the temperature increases to 100 K, local modes and Raman processes become prominent, and T_1 decreases to ranges between 0.3–6.0 μs [85]. Similarly, T_m ranges between 2.3–4.7 μs at approximately 9 K, but at 100 K, T_m decreases to 0.8–2.0 μs due to the increase in local motions and spin–lattice relaxation [85]. For dHis-Cu(II) labeled biomolecules T_1 and T_m have been found to be ca. 350 ms and 3.5 μs, respectively [86], which limits practical distance measurements to approximately 4 nm.

To determine the cumulative effects of temperature, amount of cryoprotectant, and spin concentration on relaxation for Cu(II) spin labels [77, 85, 87, 88], systematic measurements were carried out [89]. Relaxation measurements were performed on the GB1 protein mutant labeled with dHis at two sites [89]. First, two-pulse relaxation measurements systematically showed that Cu(II) concentrations between 20–800 μM have a minor effect on T_m. Using 40% (w/v) glycerol as the sample cryoprotectant [87] and operating at 18 K are also ideal to maximize T_m. Under these conditions a T_m of 4.1 μs is achievable depending on the labeled sites. Using these optimized parameters, the impact of coupled electron–nuclear interactions on T_m was dampened, but not substantially reduced.

Another attractive method to increase relaxation times is to deuterate protons to reduce the electron nuclear dipolar interactions [83, 90–93]. These effects are

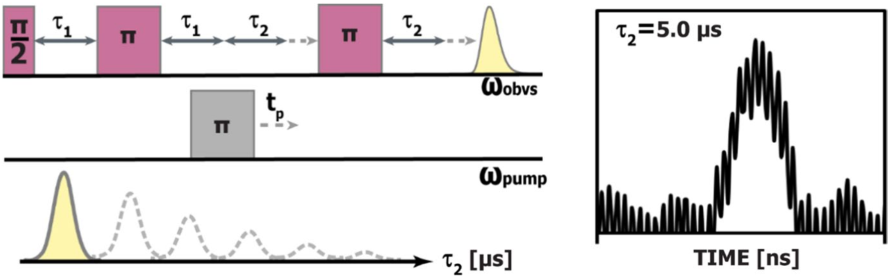

Fig. 5 Example of the DEER pulse sequence. The refocused echo (yellow) intensity and area decreases as τ_2 is increased to measure longer distances. The reduction in echo magnitude is due to relaxation processes to which Cu(II) is susceptible, such as electron–nuclear interactions and nuclear spin diffusion. The right panel shows the refocused echo in a Cu(II)–Cu(II) DEER experiment at a 5.0 μs dipolar evolution time. Longer distances requiring a long τ_2 are impractical due to the low signal to noise. (Color figure online)

illustrated in Fig. 6 which shows echo decays obtained on 6H/8H GB1 under various conditions.

Figure 6B shows echo decays for Cu(II)-labeled GB1 with naturally abundant His and d_5 His in naturally abundant solvent. In Fig. 5B the difference in T_m between the d_5 His (pink) and wildtype samples (black) is 180 ns with clear modulation from deuterium present in the d_5 His signal. Thus, replacement of the ten side-chain protons with deuterium enhances relaxation by ca. 180 ns. This result is in remarkable agreement with recent work that approximates a T_m enhancement of 28 ns per proton within 0.4–0.8 nm and 7 ns per proton within 0.2 nm—for a total of 196 ns

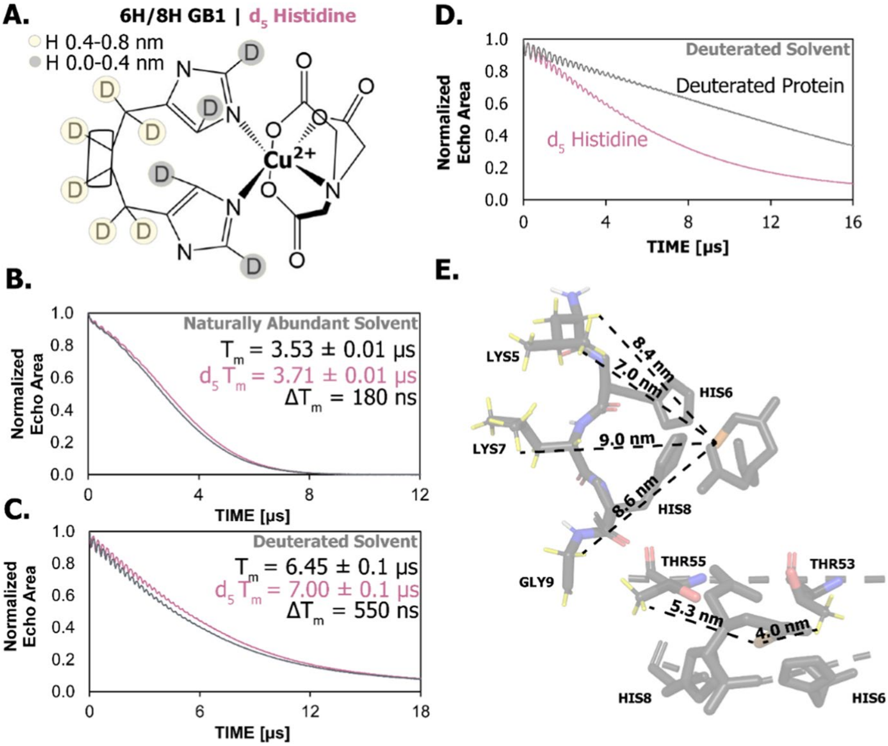

Fig. 6 **A** Representation of histidine proton locations and their respective distances from the Cu(II) center for dHis. Two-pulse echo decays for **B** naturally abundant (black) and d_5 histidine (purple) 6H/8H mutant labeled Cu(II)–NTA in water, buffer, and 40% glycerol **C,** naturally abundant and d_5 histidine Cu(II)-labeled GB1 in deuterated water, buffer, and 40% d_8 glycerol and **D** fully deuterated and d_5 histidine Cu(II)-labeled GB1 in deuterated water, buffer, and 40% d_8 glycerol. The T_m increases by 180 ns by deuterating histidine and 550 ns in deuterated solvent. **E** Protons within 0.4–0.8 nm of Cu(II) from neighboring residues (top) or from adjacent beta sheets (bottom). The T_m for d_5 His is still shorter than a fully deuterated proton due to presence of protons from neighboring residues and β-sheets. The dHis labeled GB1 samples were prepared to 75 μM protein and 150 μM Cu(II)–NTA. Echo decays were obtained using a two-pulse sequence π/2–τ–π–τ–echo with a π/2 pulse of 12 ns, π of 24 ns, and a 8 ns τ step size, at a attenuation of 0 dB. Values of T_m were obtained by fitting the echo decays with the stretched exponential $I(t) = I(0) \times e^{-\left(\frac{\tau}{T_m}\right)^x}$. Adapted with permission from Casto et al. [89]. Details of data collection, analysis, and expression of the Cu(II)-labeled deuterated GB1 samples are provided in S.I. (Color figure online)

[91]. Figure 6C shows the echo decays in deuterated solvent for both proteins. Note the dramatic increase in T_m and ΔT_m! The increase in T_m is due to the removal of the bath of solvent protons and exchangeable protons that are in the vicinity of 0.4–0.8 nm from the spin center [94]. In addition, the ΔT_m is larger in deuterated solvent possibly because protons within 0.2 nm of other protons have a large impact on T_m [94]. The effect of these proton clusters on T_m has been shown to be cooperative, not strictly additive, and scales non linearly with relative proton concentrations [94]. Therefore removing proton clusters near Cu(II) with d_5 His, adding deuterons at the exchangeable His proton sites, and using deuterated glycerol cumulatively has a greater effect on ΔT_m than using d_5 His in isolation.

However, there still exist non-exchangeable protein protons within 0.4–0.8 nm—some of these are methyl groups on the adjacent sheet are shown in Fig. 6E. Previous work has shown that nuclear electron couplings with protons and tunneling from methyl groups in close proximity to the spin center have significant impact on T_m at low temperatures [95–98]. Figure 6D compares the echo decay for d_5 His and a fully deuterated GB1 protein. Clearly protein deuteration has a dramatic effect on T_m by removing the dHis protons and protons within 0.4–0.8 nm on neighboring residues.

Figure 7 shows the DEER echoes obtained at various conditions of isotopic abundance for GB1 labeled with dHis at two sites. As seen in Fig. 7A, at naturally abundant conditions the refocused DEER echo falls below the noise level at

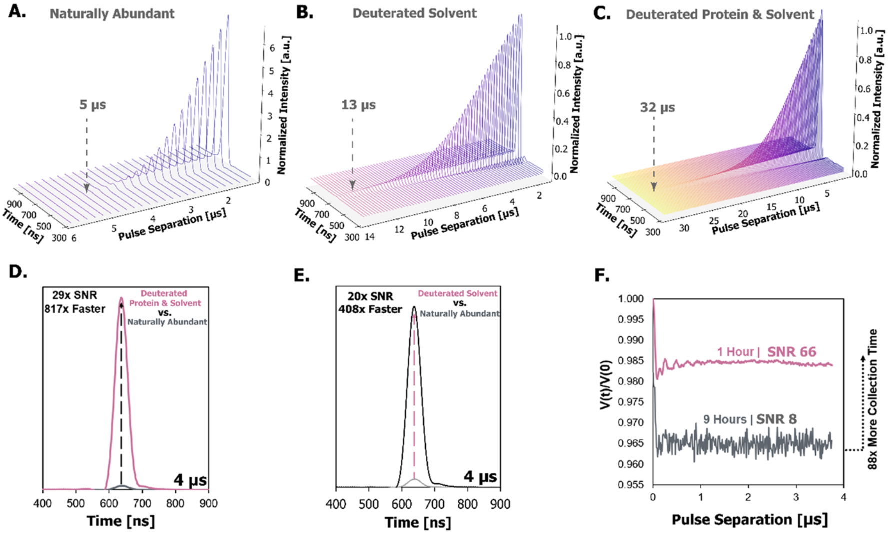

Fig. 7 Effects of deuteration on the refocused DEER echo for distance measurements. All echoes were obtained at 150 µM Cu(II), 75 µM 15H/17H/28H/32H GB1, pH 7.4, 50 mM MOPS, and 40% glycerol. The normalized DEER echo as a function of DEER pulse separation in **A** naturally abundant protein and solvent, **B** naturally abundant protein and deuterated solvent, and **C** deuterated protein and deuterated solvent. The DEER echo was collected every 200 ns over the course of the pulse separation time. DEER echo comparisons at 4 µs between **D** the deuterated protein and solvent and **E** the naturally abundant sample and deuterated solvent and naturally abundant samples as shown. **F** DEER measurement of the fully deuterated and naturally abundant samples at a 4 µs dipolar evolution time. The gain in sensitivity is clearly apparent. Adapted with permission from Casto et al. [89]

approximately 5 µs. In Fig. 7B, when the solvent is replaced with deuterated water and d_8 glycerol, the echo remains above the noise level until 13 µs. When the protein is deuterated to remove the remaining protons from the sample, an estimated T_m of 15 µs is observed and the DEER echo lasts for ca. 32 µs [89]. By exploiting deuteration, Cu(II)–Cu(II) distance measurements up to 9 nm are feasible!

The gains in sensitivity using deuteration cannot be understated. Figure 7D compares the refocused DEER echo at 4 µs between naturally abundant and thoroughly deuterated samples. The deuterated sample echo has a 29 times higher signal-to-noise (SNR) than the naturally abundant echo. The drastic difference in SNR translates to a ca. 800 times faster data collection. If deuteration of the protein is not practical, then as shown in Fig. 7E, using only deuterated solvent and glycerol provides significant gains in SNR as well. Figure 7F shows that a 4 µs DEER can be quickly obtained in under an hour using deuteration in place of naturally abundant samples.

3.2 Broad EPR Spectrum Challenges

A second limitation for Cu(II)-based PDS is that rectangular pulses have a finite bandwidth of excitation. Figure 8 depicts the field swept electron spin echo spectra of Cu(II) and nitroxide at Q-Band. The simulated excitation profile of a 24 ns rectangular pulse is overlayed on the spectra. The pulse covers a significantly smaller portion of the Cu(II) spectrum since the spectrum is 18-fold broader than nitroxide at Q-Band [99]. A narrow bandwidth of excitation leads to a fraction of the spin excited for Cu(II) compared to nitroxide. In turn, the oscillations of the dipolar frequency observed in PDS have shallow modulations. Figure 8 shows a simulated Cu(II) time domain signal with shallow modulations compared to a simulated nitroxide measurement. In return, longer data-collection times are necessary to achieve sufficient SNR to differentiate the modulating signal from the noise to confidently interpret distances [100].

The depth of the time trace modulations, λ, depends on the number of excited spin pairs [101] Fig. 8 shows how λ is quantified from a background subtracted time trace. Thus λ is a valuable parameter to determine spin-labeling efficiency

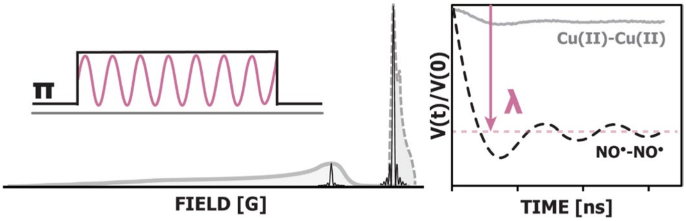

Fig. 8 Comparison of the detected field swept EPR spectra of Cu(II) and nitroxide at Q-Band. The excitation profile of a 24 ns rectangular pulse is overlaid on each spectra. The pulse covers only a fraction of the Cu(II) EPR spectrum compared to nitroxide. The right side of the panel shows simulated oscillating time domain signals for Cu(II) and nitroxide based PDS measurements. The limited excitation of the Cu(II) spectrum results in a PDS measurement with shallow modulations. Thus the modulations for Cu(II) can be more easily obscured by noise. The depth of the modulation is quantified by the modulation depth parameter, λ

and monitor biomolecule complex assembly [102]. In PDS measurements, the SNR is conventionally defined as λ divided by the RMSD of the time trace noise (σ_{Noise}) [103]. Accordingly, exciting a greater portion of the Cu(II) spectrum will considerably increase λ for enhanced sensitivity [8].

$$\mathrm{SNR} \approx \frac{\lambda}{\sigma_{\mathrm{Noise}}} \tag{1}$$

Increasing the number of excited spin pairs was conventionally limited by the pulse lengths. Traditionally, rectangular pulses at a fixed frequency are used for PDS measurements (cf. Fig. 9A). The shorter the length of a rectangular pulse the larger the excitation bandwidth. The bandwidth of excitation for such pules is often limited by the amplifier and in the case of double resonance experiments sometimes by the bandwidth of the resonator. Fortunately, the advent of pulse shaping technology in EPR has provided a new avenue [104–109]. With arbitrary waveform generators, rectangular pulses can be replaced with frequency-sweeping shaped pulses [110, 111]. Figure 9B depicts how a frequency-swept pulse changes frequency over the pulse duration, which increases excitation bandwidth. Frequency-sweeping pulses excite a larger fraction of the Cu(II) EPR spectrum than rectangular pulses, improving λ and sensitivity [8]. These alterations to pulse shapes allow for a user defined bandwidth and dramatically improves pulse excitation profile breadth and uniformity.

Systematic sensitivity measurements for DEER on Cu(II)-labeled protein and DNA (c.f. Fig. 9E and F) with frequency-swept pump pulses using a commercial Bruker spectrometer, arbitrary waveform generator, and resonators have been reported [86]. In this work a 200 MHz chirp pump pulse was used in DEER to maximize the bandwidth while remaining within the capacity of the Bruker resonators and the SpintJet AWG. Figure 9C compares the experimentally measured pulse inversion profiles using the MD5 X-Band resonator. The excitation bandwidths of a rectangular pulse and chirp pulse are overlaid on Cu(II) EPR spectrum in Fig. 9D to exemplify the drastic increase in excitation bandwidth with a frequency-swept pulse.

Figure 9E and F shows that using a chirp pump pulse with a 200 MHz bandwidth increases the modulation depth of DEER by as much as four-fold for Cu(II) labels at Q and X-Band. Remarkably a λ of 18.3% at X-Band is easily achievable. For long-range distance measurements above four nm a chirp pulse drastically increases sensitivity and reduces collection times from days to hours. Such reductions are more modest for short distance measurements since these require shorter chirp pulses [8]. Further gains are likely achievable by optimizing the profile of frequency-swept pulses to remove deviations caused by instrumental imperfections [106, 112, 113] and by adopting arbitrary waveform generators and resonators with greater bandwidth [114, 115]. Indeed, modulation depths of 44% at X-Band and 35% at Q-Band have been reported with custom resonators [8].

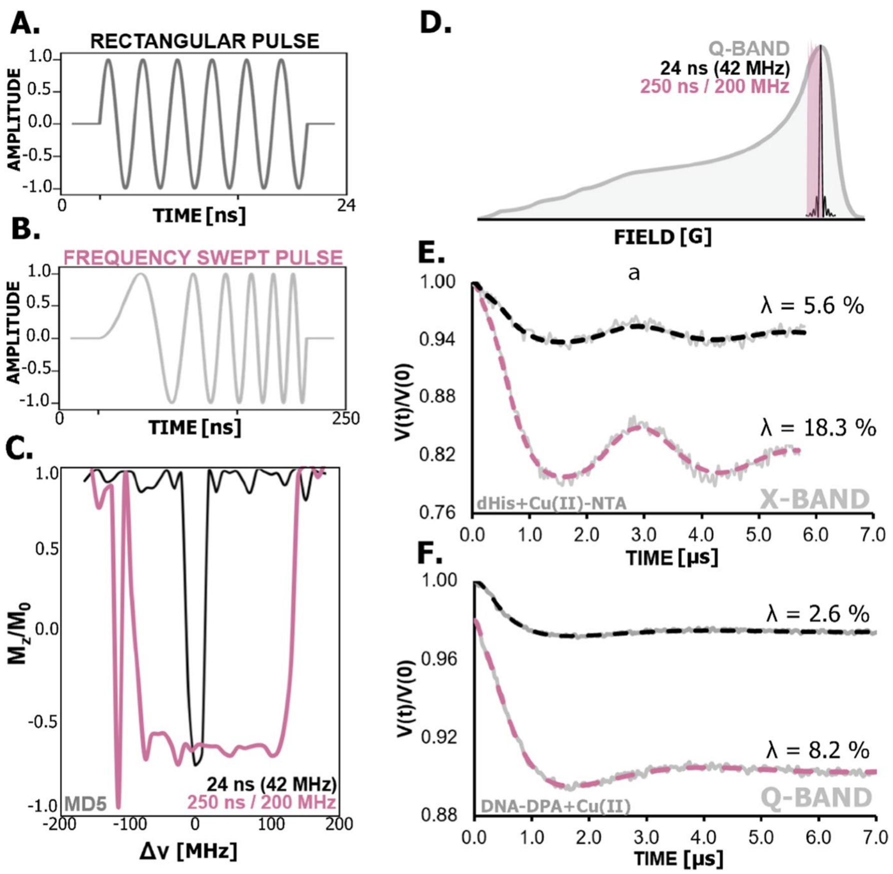

Fig. 9 Cartoon representation of **A** a rectangular pulse with a fixed frequency over a set duration and **B** a frequency sweeping pulse that changes frequency over a set duration. **C** Experimentally collected spin excitation profiles for a 24 ns rectangular pulse (black) and 250 ns frequency sweeping pulse with a 200 MHz bandwidth (purple) from a Bruker MD5 resonator. The dip at −100 MHz is likely due to either resonator-bandwidth limitations or hardware effects that are distorting the pulse and the resulting excitation profile. **D** Echo detected Cu(II) field sweep at Q-Band overlayed with the experimental excitation profiles from **C**. **E, F** Cu(II)–Cu(II) DEER comparison between a 24 ns rectangular pulse (black) and 250 ns/200 MHz Chirp pulse at X-Band with the MD5 resonator and Q-Band with the Bruker QT2 resonator as shown. Adapted with permission from Casto et al. [86]. (Color figure online)

3.3 Orientational Selectivity Challenges

Limitations in pulses lengths can also lead to another complication for Cu(II)-based PDS measurements. At a given magnetic field only a small fraction of spins are excited, which can lead to a phenomenon called orientation selectivity [28, 116, 117]. Figure 10 illustrates this effect using a hypothetical case where the $g_{||}$ axis of two Cu(II) spins are exactly aligned and oriented perpendicular to the interspin vector. In this case, performing the PDS measurement at the maximum of the FS-ESE spectrum (c.f. point III in Fig. 10) excites $g_{\perp}$, leading to a preferential sampling

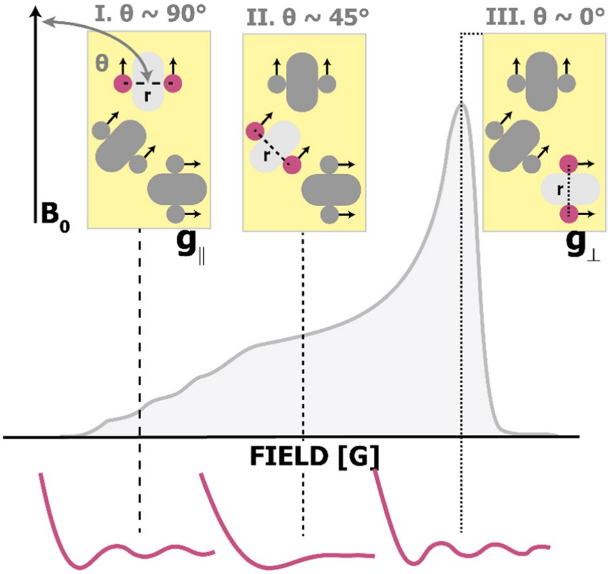

Fig. 10 (Top) Cartoon representation of an orientational selective measurement where only some spin pairs in "test tube" are excited at each magnetic field. At the lowest field the $g_{||}$ for both spins are excited for this protein leads to a preferential excitation of $\theta = 90°$ (point I). The angle θ describes the angle of interspin vector r to the applied magnetic field B_0. The proteins blocked in dark grey have g-tensors that are not selected at that magnetic field and are preferentially excited elsewhere in the spectrum. (Bottom) When only a subset of spin label orientations are excited the distance measured may differ depending on the magnetic field the experiment was performed at. In orientationally selective PDS measurements, the relative g-tensors between spin pairs are narrowly distributed throughout the spectrum. In return, only a subset of θ may be detected at different regions in the EPR spectrum. Since the oscillating signal in PDS depends on $\frac{3cos^2\theta-1}{r^3}$, the period of the time trace and resulting distance then changes with magnetic field. Up to 17 different measurements have historically been necessary to obtain an orientationally averaged distance measurement. (Color figure online)

of interspin vectors, r, that are aligned with the magnetic field (i.e. $\theta \sim 0°$). On the other hand, θ values of ~ 90° are sampled in the $g_{||}$ region of the spectrum (cf. point I in Fig. 10A). Since the oscillating signal in PDS depends on $\frac{3cos^2\theta-1}{r^3}$, the period of the time trace then changes with magnetic field. Given that the relative orientations between the Cu(II) centers is an unknown a priori, this can introduce a complication for Cu(II)-based PDS measurements.

Such effects are somewhat mitigated by orientational flexibility in several systems. For example, the nitroxide label R1 has five flexible bonds that broadly distributes the relative g-tensor orientations of spin pairs in the EPR spectrum. In addition, the hyperfine interaction further helps mitigate orientation effects. Thus, all θ values can typically be sampled at one field at X- and Q-Band. Nevertheless, orientational selectivity has been observed in instances where the nitroxide label is restricted [118–122].

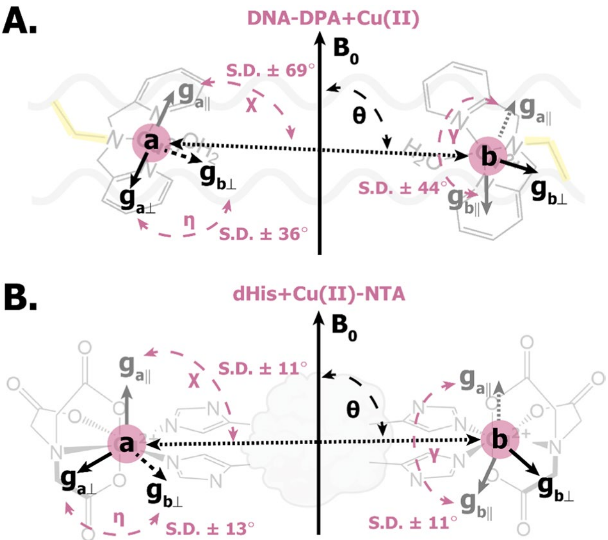

Fig. 11 Cartoon representation of relative g-tensor orientations between paired spins for **A** DNA-DPA and **B** dHis. The angles χ, η, and γ characterize the relative g-tensor orientations. The standard deviations for each angle were estimated from MD simulations and quantum mechanical calculations with MDTraj. The standard deviation of the angles correlates with the distribution of the relative g-tensor orientations throughout the EPR spectrum. Large standard deviations allow more g-tensor orientations to be sampled in a measurement, and therefore reduce orientation selectivity effects. **A** The two flexible bonds in the yellow linker are primary sources of the large standard deviation of relative g-tensor orientations for the DNA label. DEER at X- and Q-Band does not exhibit orientational selectivity because of the large orientational distributions. **B** The dHis label does not have a flexible linker to the protein and therefore the standard deviation of the three angles is largely dependent on the fluctuation of the Cu(II) coordination environment throughout the ensemble. The dHis label is not orientationally selective at X-Band but can be at Q-Band. DNA and protein cartoon scaffolds were made using Biorender. (Color figure online)

Similarly, the Cu(II)-DPA DNA label, shown in Fig. 11A, is flexible and not orientationally selective at X- and Q-Band [123]. Figure 11A shows paired Cu(II) DNA labels, g-tensor orientations, and the three angles χ, η, and γ that characterize the relative g-tensor orientations between the spins. Estimates of the standard deviations of the three angles estimated from MD simulations and QM calculations are also shown [124, 125]. The standard deviation of the angles correlates with the distribution of the g-tensor orientations in the EPR spectrum. Therefore large standard deviations of the angles make sampling all g-tensor orientations practical at one magnetic field [116]. Here we see the standard deviation of the relative g-tensor orientations is large and ranges from an estimated 36° to 69°. The origin of such orientational distribution has two main contributors. First, the bond angles and bond lengths of the Cu(II) to coordinating DPA are elastic. For example, MD simulations on labeled DNA indicates that the bond length can range from 1.9 to 2.3 Å [124]. In addition, these simulations suggest the torsional angles of the Cu(II)-N bonds vary between −98° and 26° [124]. Quantum mechanics (QM) calculations based on these results suggest the DPA coordination environment of Cu(II) results in an estimated standard deviation of 25° between relative g-tensor orientations [124]. In addition, there exist two rotatable bonds that link the label to the backbone. Fluctuations in these bonds help to increase the standard deviation of the g-tensor orientations up to 69° [124]. This large standard deviation allows proper sampling of all label orientations in a single measurement.

On the other hand, dHis does not possess a flexible linker like R1 or the DNA Cu(II) label. Therefore the relative g-tensor distribution is solely dependent on the fluctuating coordination environment of the Cu(II)–N bonds [116, 126]. Figure 11B shows that the three angles for dHis have a standard deviation estimated by MD and QM calculations ca 12° [126]. Experimental estimates have also been reported recently [127]. These results agree well with the values approximated from the molecular dynamic simulations. As such, the distribution of g-tensor orientation in the Cu(II) EPR spectrum is relatively narrow. This orientational distribution is sufficient to wash out orientational selectivity at X-Band [126]. However, the sparse distribution of g-tensor orientations can give rise to orientational selectivity at Q-Band [126, 128]. As a result, up to 17 DEER measurements at Q-Band were acquired in initial work on a rigid protein to obtain distance information reflective of the entire ensemble [129]. Requiring additional measurements for one sample increases data-collection time and puts a physical bottle neck on the ability to rapidly run experiments.

In response, the conceptual basis of Cu(II) DEER was systematically explored to develop optimized acquisition schemes that reduce the number of measurements [128]. Figure 12 depicts the optimal acquisition scheme for dHis to rapidly obtain an orientationally averaged distance measurement. By utilizing a pump pulse (ω_p)

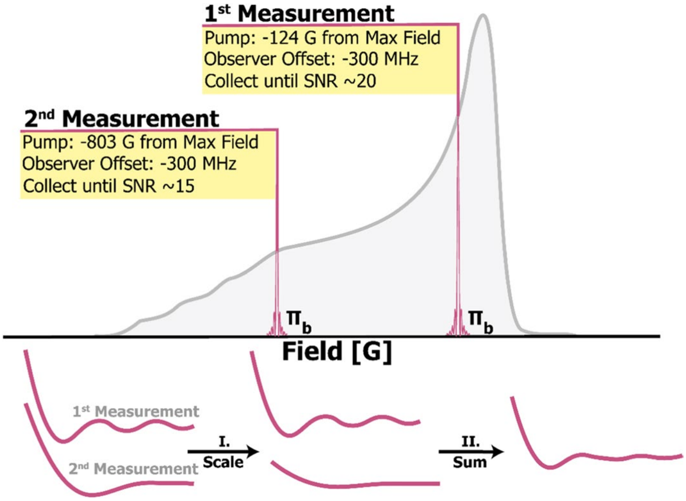

Fig. 12 (Top) Depiction of the strategic acquisition scheme for dHis to obtain an orientationally averaged distance with measurements at only two fields. Experiment configuration details are in the yellow boxes. (Bottom) To obtain the orientationally averaged distance measurement first normalize both time traces to 1.0. Next, scale each time trace to the intensity of the pump-field position relative to the maximum field of absorption, then sum them. (Color figure online)

that is—300 MHz offset from the observer frequency (ω_0) at the two fields shown, all orientations are efficiently sampled in two measurements. The SNR benchmarks shown are based on data presented later in the review. To further increase sensitivity, a frequency sweeping pulse can also be incorporated −300 to −100 MHz from the observer frequency [130]. If a 300 MHz offset is not achievable then a third measurement may be required. More details of theory and concepts are available elsewhere [116, 128, 130].

Once the data are acquired at the two fields, each measurement is first normalized 1.0. The two measurements are then scaled with respect to the relative intensity at the observer fields. Scaling is necessary to ensure the final time trace accurately represents the populations of distances in the ensemble that make up the final distribution. After scaling, the time traces are then summed to produce the orientationally averaged measurement. Note that most analysis programs that extract distance distribution from PDS data use nitroxide g-factors. For Cu(II) the appropriate g-factor for the Cu(II) label must be used [127, 131, 132]. This strategic acquisition scheme allows Cu(II) labels to take advantage of the enhanced increase in sensitivity afforded by the use of deuteration and shaped pulses at Q-Band [133, 134].

3.4 Challenges Ameliorated

Cumulatively the use of deuteration, chirp pulses, and optimized acquisition schemes have significantly increased Cu(II) PDS sensitivity to enable the capture of short-range distances in minutes and long-range distances in hours. Figure 13 exemplifies the dramatic leap in Cu(II)-based PDS sensitivity. Figure 13A shows that between 2018–2020 a 2.3 nm distance DEER measurement on 1 mM of protein labeled with dHis required 15 h and 17 different collections. Figure 12B shows that recent Cu(II)-label method development has reduced data-collection time on 100 µM of protein to only an hour with two measurements. Notably, Fig. 13C highlights that a distance measurement in the range of 6 nm, that was not feasible in 2018, is possible in under a day.

Table 2 outlines general collection times required to achieve SNR benchmarks for 50 µL of 100 µM protein and 200 µM Cu(II) label using the DEER at Q-Band. For a 1.2 µs DEER, which is suitable for two periods of a 3.3 nm distance, an SNR of 83 is achieved in approximately an hour. An SNR of 83 is over three-fold higher than the community recommended SNR benchmark of 20 for reliable distance determination [100]. In addition, a 7.0 µs dipolar evolution that accommodates a 6 nm distance, reaches an SNR of 20 in under a day.

The accuracy of the distance distribution is affected by the SNR of the time trace [135]. For broader distance distributions, a higher SNR than the community benchmark of 20 [100] may be preferable since the broader dipolar oscillations can be more difficult to discern from the noise at a lower SNR [135]. This issue highlights another benefit of the dHis label. The size and rigidity of dHis label leads to narrow distributions that generate well resolved oscillations in the time trace. Although these collection times in Fig. 13 and Table 2 are for dHis, these advancements in

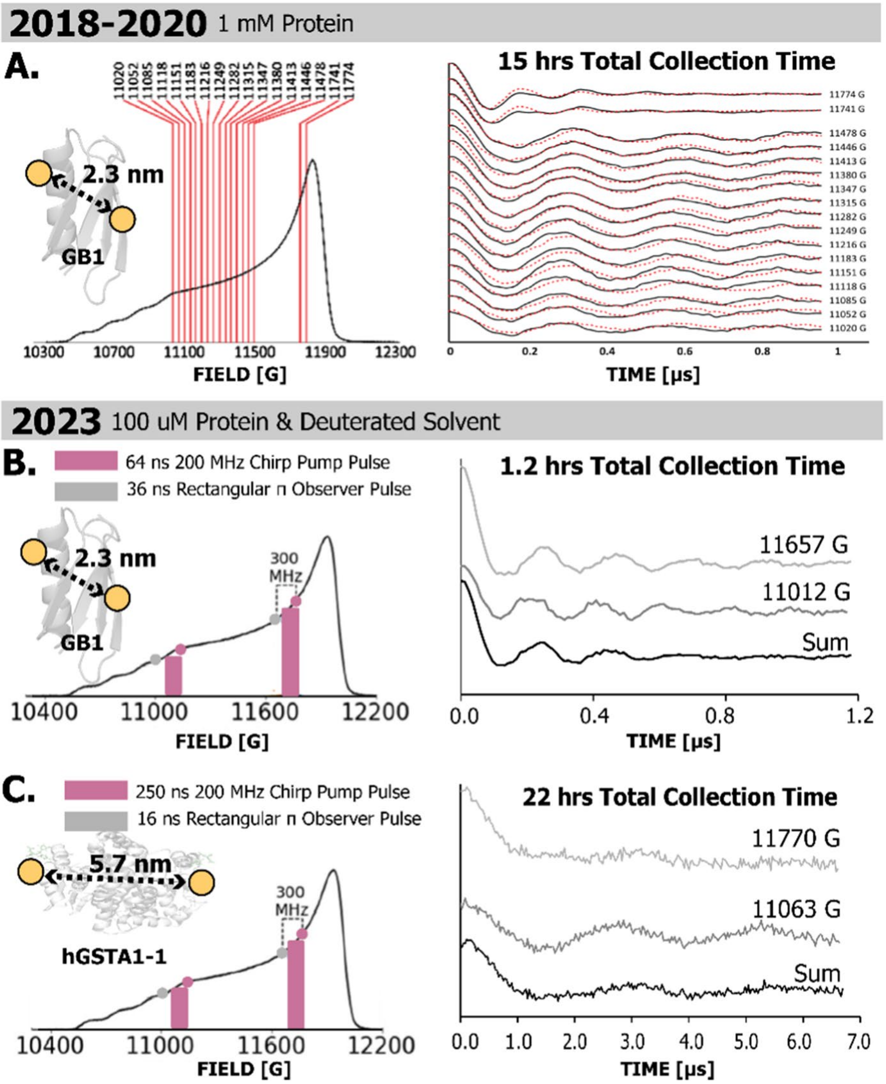

Fig. 13 **A** Between 2018–2020 Cu(II)–Cu(II) Q-Band distance measurements with the dHis motif required up to 17 measurements over 15 h of collection for a 1 mM protein sample. Adapted with permission from Gamble Jarvi et al. [129]. As of 2023 Cu(II)–Cu(II) Q-Band measurements using shaped pulses, strategic acquisition schemes, and deuterations can obtain **B** 3 nm and **C** 6 nm range distances in 1.2 h and 22 h, respectively on 100 µM protein and 200 µM Cu(II) samples. Adapted with permission from Hasanbasri et al. [130]

Table 2 Calculated DEER data collections time for SNR from data shown in Fig. 13B, C

Dipolar evolution time (μs)	Field 1 collection (h)	Field 1 SNR	Scans	Field 2 collection (h)	Field 2 SNR	Scans	Total collection (h)	Sum SNR
1.2[a]	0.25	73	2	0.25	26	2	0.50	68[c]
1.2[a]	0.50	98	4	0.70	31	6	1.2	83
7.0[b]	6.3	21	18	16	15	45	22	23

The data presented were previously published in Hasanbasri et al. [130] and is adapted for this work with permission

[a] 1.2 μs: 117 points, 20 SPT, 1500 μs SRT, 8-step tau suppression, 16-step phase cycling each scan

[b] 7.0 μs: 266 points, 20 SPT, 1500 μs with 10-step tau suppression, 16-step phase cycling each scan

[c] Calculated by summing fewer data collection scans of the data previously published in Hasanbasri et al. [130] until the lower field reached the community benchmark SNR of 20 [100]. The original data had a SNR of 83 and took 1.2 h

method development are generalizable and applicable to other Cu(II) systems in the solution state such as the Cu(II) DNA label. The leap in Cu(II) PDS sensitivity has greatly expanded the scope of feasible biological applications for Cu(II)-based distance measurements.

4 Biological Applications

Since EPR generally provides sparse constraints, the technique does not naturally lend itself to the de novo prediction of protein structure, although there are some examples in literature [136, 137]. On the other hand, the measurement of few distances is sufficient to elucidate induced conformational changes, [138–146] the relationship between site-specific dynamics to function, [147–152] the relative arrangements of biomolecules, [153–155] quaternary packing, [118, 156, 157] or substrate/metal associations, [19, 158–160] and the discrimination between structural models [161–164]. Much of this work is also aided by close coupling of experiment constraints with modeling [165–171]. Furthermore, the sensitivity of EPR coupled with the ability to measure protein structure and dynamics in membranes and even in-cells have made EPR especially relevant [48, 49, 172–175]. The union of enhanced sensitivity and robustness of Cu(II) labels has been pivotal for biological applications. The preciseness and rigidity of dHis has provided insights into not only conformational changes but also nanomolar equilibrium constants, protein assembly, subunit orientations, and site-specific dynamics. Figure 14 summarizes some of the applications of Cu(II) spin labeling.

4.1 Induced Conformational Changes

The dHis motif has delineated structural transitions of the detoxification enzyme glutathione s-transferase (hGSTA1-1) [176, 177] upon the binding of ligands [178]. Figure 14A shows the two α9 helices that coordinate ligands in hGSTA1-1. The

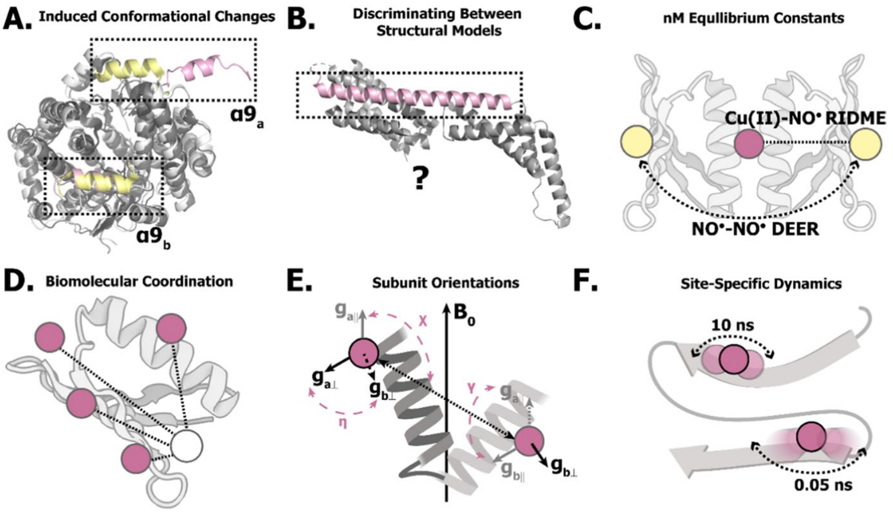

Fig. 14 Cartoons of biological applications using Cu(II) spin labels. Illustrations were primarily made using Biorender. **A** Combining dHis distance constraints with Weighted Ensemble MD discerned the seconds timescale conformational change of homodimer hGSTA1-1 upon coordinating ligand. The α9 helices go from partially delocalized (pink), to fully localized (yellow) via a negativity cooperativity mechanism to bind ligand. [PDB: 1K3L]. Adapted with permission from Bogetti et al. [178]. **B** Crystral structure of the guanine nucleotide dissociation inhibitor domain (GDI) of *Yersina* outer protein O (YopO). The α14 helix highlighted in pink is linear when actin is absent [PDB: 2H70]. When actin is present, the crystal structure shows the α14 adopts a bent confirmation [PDB: 4CI6]. EPR measurements using nitroxides and trityl spin labels gave bimodal distributions of free YoPO. The bimodality suggests linear and bent YoPO coexists in solution. Measurements using dHis show only one conformation of the YoPO helix in solution without actin. **C** Orthogonal nitroxide and Cu(II) labels combined with RIDME offer robust sensitivity to determine nM equilibrium constants for metal ion coordination and protein dimerization [PDB: 2J52]. **D** Cu(II)-based EPR can precisely report on biomolecular coordination, such as native protein coordination to metal ions. The native Cu(II) binding site of GB1 was determined via trilateration with four dHis distance constraints. PDB: 2J52. This methodology can be extended to discern bimolecular assembly. **E** Cu(II) orientational selectivity at Q-Band can be exploited to determine changes in subunit orientations. On the cartoon protein the g-tensors for each spin label are shown. Projection of g-tensors from the paired spin are shown as dashed lines for ease of comparison. The angles χ, η, and γ shown are used to quantify the relative g-tensor orientations between spins. These angles can be found by simulation of orientationally selective dipolar signals to determine the orientations of the spins. **F** Cu(II) labels can also report protein site specific dynamics on the ns timescale. This technique using dHis is sensitive to α-helix and β-sheet dynamics without perturbation from adjacent residue sidechains. (Color figure online)

distance between the two helices was found to decrease, and the distribution narrowed with increasing amount of ligand. This provided the first structural insights into the unliganded and partially liganded states of hGSTA1-1 to complement existing information on the liganded state from X-ray crystallography [179].

Even more importantly, the insights from the EPR data were used to guide enhanced sampling MD simulations using an unbiased weighted ensemble (WE) approach [180–182] to generate a hGSTA1-1 transition pathway from the unliganded to liganded state [183]. Remarkably, these simulations show that only one of the two α9 helices (one in each subunit) in the dimeric protein is undocked at a time in the unliganded state and ligand binding leads to the docking of this helix. Figure 14A shows the dominant conformation in the unliganded state — in this conformation one of the α9 helices is undocked and the other is docked (pink). In contrast, both α9 helices become docked in the presence of increasing ligand concentration (yellow). Thus, the protein functions by a mechanism that involves negative cooperativity. This work also shows how function-associated large amplitude conformational changes that occur on the seconds timescale can be resolved at an atomistic level by a combination of EPR and enhanced sampling MD simulations.

With respect to DNA, the DPA Cu(II) label was used to reveal conformational changes in DNA that help *E. coli* survive under high concentrations of toxic Cu(I). The fundamental cellular process that initiates defense is shown in Fig. 15A. The copper efflux regulator protein (CueR) in *E. coli* binds to Cu(I) with zeptomolar affinity [184] and bends the DNA [185–188]. This bending allows the RNAp to access the DNA and express proteins that remove Cu(I) from the cell [189–195].

Point-to-point distance measurements were performed on labeled DNA as a function of protein and Cu(I) concentration to DNA [185]. These constraints are incisive since the Cu(II) label provides precise distance measurements within an estimated 0.1–0.2 nm of the DNA backbone constraint [27, 124]. Figure 15B shows the measured distance distributions for the DNA, the protein–DNA complex, and the protein–DNA complex in the presence of Cu(I). At low-protein concentrations with Cu(I), the most probable distance decreases relative to the free DNA, indicating the DNA is being bent. This observation is consistent with crystallography and cryo-EM structures [190, 194, 195].

The results in the absence of Cu(I) are more notable. At low-protein concentrations the distribution broadens but the most probable distance of the protein–DNA complex remains similar to the free DNA. The DNA remaining undistorted in the protein–DNA complex has been suggested by crystallography data obtained with a ratio of 1:2 protein to DNA [190]. Remarkably, however, we found that at high concentrations of protein the distance decreases, which suggests the Cu(I)-free protein can also bend the DNA!

The EPR data provides crucial insight into the deactivation of the CueR defense response. Figure 15C depicts a cartoon of the hypothesis for the CueR deactivation mechanism. At high Cu(I) concentrations, a large amount of CueR is produced via a copper sensing mechanism [187, 188]. This leads to the Cu(I)-bound protein bending the DNA in order to express genes that remove the metal ion. Once homeostasis is restored, however, the gene expression must be terminated. Given that Cu(I) binds to CueR at zeptomolar affinity [184] it is unlikely the Cu(I) will dissociate from the protein–DNA complexes which are still promoting the expression of Cu(I) defense proteins. However, the excess CueR that was produced in high quantities still remains in the cell. Since Cu(I)-free CueR can bind to bent DNA, it is kinetically and thermodynamically straightforward for Cu(I)-free protein to replace Cu(I)-bound CueR on the bent DNA. After CueR concentrations return to cellular equilibrium the complex likely dissociates or unbends the DNA [196]. This substitution therefore stops the production of Cu(I) defense proteins. The EPR data thus provide key structural details to a direct substitution pathway for termination that was

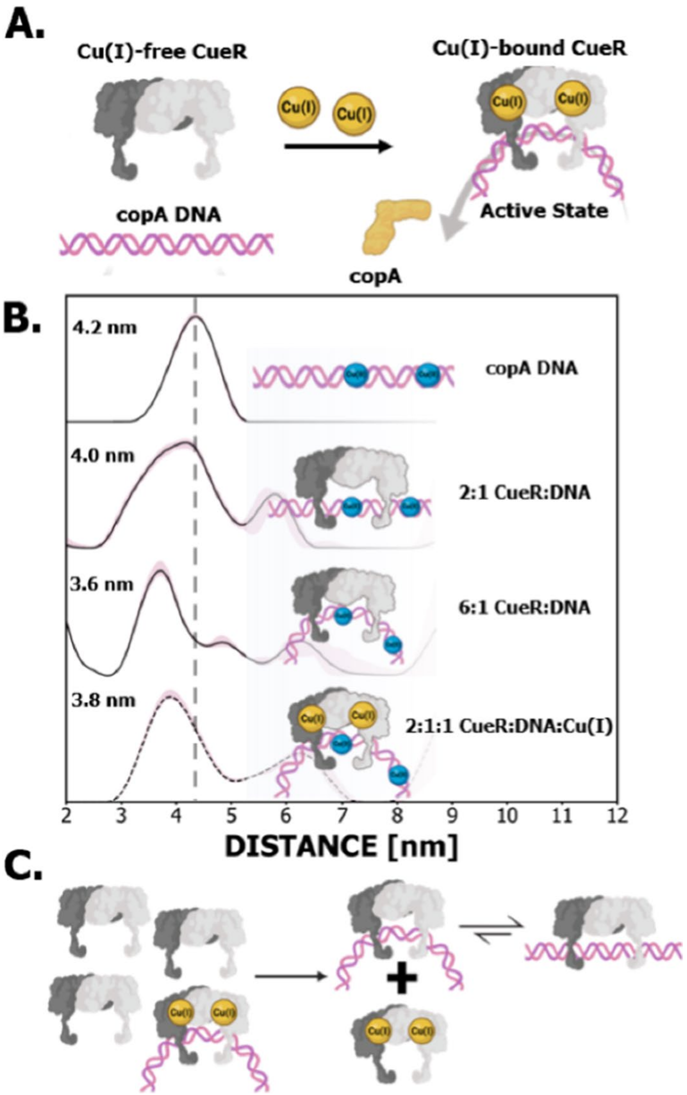

Fig. 15 **A** A simplified cartoon representation of the CueR defense mechanism where CueR coordinates to DNA under high Cu(I) stress. Cu(I)-bound CueR bends the DNA to allow RNAp to transcribe defense proteins that remove Cu(I) from the cell. **B** Distance distributions for the CueR–DNA complex under varied protein and Cu(I) concentrations as shown. The DNA distance constraint decreases in the presence of excess CueR or low concentrations of Cu(I). **C** Proposed transcription termination pathway where the excess Cu(I)-free CueR produced to defend the cell substitutes and removes the Cu(I)-bound CueR from the active complex. After substitution, DNA can return to an undistorted state or dissociate from the complex. Adapted with permission from Casto et al. [185]. Figure illustrations were created with Biorender

originally inferred by kinetic measurements using smFRET [184, 196]. In summary, missing structural details of the CueR defense mechanism were elucidated here by monitoring a single Cu(II)–Cu(II) constraint in DNA as protein and Cu(I) concentrations were varied [185].

In addition, distance constraints were obtained on dHis labeled CueR in the presence of different concentrations of Cu(I) [197]. This work provided structural evidence of two different active-state conformations for Cu(I)-bound CueR coordinated to DNA. The presence of two active-state conformations was also inferred by smFRET kinetics work [189]. Note, that flexible nitroxide labels with distance distributions up to five times broader than dHis were not able to resolve two different active-state conformations in similar measurements [191]. The EPR constraints combined with elastic modeling indicate at low Cu(I) concentrations the CueR binding helices are more compressed on the DNA than at high Cu(I) concentrations [197]. On the other hand, the high Cu(I) model is in agreement with available crystal structures [190]. One conformation binding the DNA more tightly structurally supports inferences from kinetic measurements using smFRET that suggest that only one conformation leads to activation while the other is a "dead end" pathway [189]. The measurement of site-specific dynamics by EPR has provided further insight into the correlation between Cu(I) binding sites in CueR and activation [193].

Together the work on hGSTA1-1 and CueR illustrates the value of EPR measurements. The elucidation of the relationship between structure and function in these proteins necessitated structural constraints at several concentrations of ligands, or metal to protein and DNA ratios. Such measurements can be prohibitive for traditional techniques due to various factors, such as the size of the complexes, low solubility in the presence of metals, and associated difficulties with crystallization, or the presence of structural fluctuations. On the other hand, a few carefully chosen distance constraints can be surgically measured and combined with modeling to provide an atomistic picture of protein structure and function.

4.2 Discrimination Between Structural Models

The rigidity of dHis is also valuable to discriminate between structural models of biomolecules obtained from different techniques. One such instance is with respect to models of the guanine nucleotide dissociation inhibitor domain (GDI) of *Yersina* outer protein O (YopO). The GDI of YopO is responsible for protecting Yersina bacteria from phagocytes [127, 198, 199].

Figure 14B shows the crystal structure of the GD1 of YoPO with the α14 helix highlighted. Crystallography suggests that the α14 helix bends in the presence of actin, while this helix is straight in the absence of actin [200, 201]. On the other hand, solution state PDS EPR using nitroxide and trityl spin labels on α14 of YopO without actin gave a bimodal distance distribution [202]. The bimodality of these results may suggest that the protein exists in both conformations in solution [202]. However, another possibility might be that the spin label side chains hold two conformations that lead to the bimodality [202]. In comparison, dHis distance measurements show only one YoPO conformation in solution [127]. The bipedal attachment of Cu(II) in these measurements, thus allows for an unambiguous interpretation of distance in terms of backbone conformation [127]! Thus PDS data can directly be compared or combined with other techniques that provide biomolecular structural information. Conversely, other spin labels that utilize flexible linkers may require further analysis to disentangle the spin label contributions from distance distributions. In addition, this work found even though YoPO has 22 native histidine residues, the Cu(II) complex specifically coordinated to the dHis motif site, which suggests that a His-null background may not be necessary for Cu(II) labeling.

4.3 Nanomolar Equilibrium Constants

The specificity of Cu(II)–NTA for dHis sites opens avenues for orthogonal labeling strategies with cysteine dependent labels such as nitroxides and trityl. Such schemes have led to improvements in the sensitivity of PDS measurements and a new methodology to measure association events [203–205]. First, techniques like relaxation-induced dipolar modulation enhancement (RIDME) rely on spontaneous flips of one spin in the coupled spin pair for distance measurements. The shorter T_1 of Cu(II) compared to nitroxide or trityl is ideal since it promotes efficient acquisition and accelerates data-collection times [206]. Second, the rigidity and size of dHis combined with nitroxide narrows the distance distribution relative to using two nitroxide or two trityl labels [207]. Indeed such narrowing can also help resolve the contribution of nitroxide or trityl fluctuations to the measured distribution width [127, 207]. Finally, the narrow EPR spectra of nitroxide and trityl can be efficiently excited and detected. Such schemes have enabled distance measurements at concentrations as low as 10 nM [208]. It has also been reported that double quantum coherence (DQC) can measure distances on a ca. 25 nM protein sample doubly labeled with nitroxides [209]. These results are particularly exciting given that most measurements are normally performed at micromolar concentrations.

Interestingly, methodology has been developed to analyze the modulation depth of the RIDME signal to measure association constants. Figure 14C shows a cartoon of a protein dimerized by the addition of Cu(II)—each protein contains a single R1-labeled site. Dimerization leads to a distinct RIDME signal. The change in modulation depth as a function of the concentration of Cu(II) was then used to measure the protein dimerization constants in different buffers [203]. A similar strategy highlighted the specificity of Cu(II)–NTA to dHis in the presence of competing ions [204]. Together these results have established a new method to measure association constants at concentration much lower than possible by isothermal calorimetry. The ability to work at nanomolar protein concentrations is vital to access binding affinity and equilibria present only in the sub micromolar regime. [210, 211] Note, however, that the measured values reflect properties at lower than room temperature.

4.4 Biomolecular Coordination

The precision and rigidity of dHis has also enhanced the resolution of methodology to discern protein assembly [212]. For example. Figure 14C shows the positioning of four different dHis GB1 sites and the native Cu(II) binding site. Distance measurements were obtained systematically between one of the dHis sites and the natively bound Cu(II). The incisive and narrow distance distributions of dHis pinpointed the native Cu(II) binding site with only four distance measurements [212]. In comparison, similar measurements using nitroxides required between 5 to 15 measurements [158, 160, 213]. This methodology can easily be extended to elucidate how biomolecules come to form functional complexes or discern quaternary structures.

4.5 Relative Subunit Orientations

In this review, we have primarily discussed Cu(II)-orientation selectivity in the context of data-collection times. However, orientational selectivity can be exploited to determine the relative orientation between spin labels, providing another dimension to distance measurements [214, 215]. Work with dHis at Q-Band has shown that the distinct dipolar signals as function of magnetic field can be analyzed to obtain the relative orientations of Cu(II) labels [127, 129]. Figure 14E shows the g-tensors for each spin on a cartoon protein and the angles χ, η, and γ that characterize the relative g-tensor orientations. In orientationally selective measurements the discrete dipolar signal at each magnetic field can be simulated to determine the three angles [216]. These angles are then used to establish the relative orientations between the spins and subunits they are attached to. Such methodology has also been used to elucidate the orientation of Cu(II) in guanine quadruplex DNA [28] and endogenous Cu(II) binding sites in proteins to refine structural modeling [19, 21, 217]. This technique can also be adapted to provide structural insight in instances where the spin labeled subunits of a protein reorient in a conformational change.

4.6 Site-Specific Dynamics

In addition to distance measurements, Cu(II) is also advantageous in determining site-specific dynamics on the nanosecond timescale in proteins [35]. Notably, due to its size, dHis is sensitive to site-specific dynamics on both α-helices and β-sheets [59, 151]. Figure 14B shows a β-sheet where the Cu(II) labeled sites detect residue specific fluctuations on the ns time scale. Such measurements of backbone dynamics on β-sheets are otherwise challenging for labels with flexible linkers since the motions of the label can be perturbed by adjacent residue side chains [218–220]. In addition, the large anisotropy of Cu(II) is beneficial for measurements of dynamics since subtle changes in the backbone fluctuations will result in proportionally large changes in the CW-EPR spectra. Therefore, Cu(II) provides enhanced resolution of measurements of dynamics for precise timescale analysis [35, 151].

This methodology has been applied to measure the dynamics of the hGSTA1-1 α-helices responsible for coordinating ligand [151]. The measurements showed two components, one of which indicated the helices were more ordered. The addition of ligand increased the proportion of the ordered component [151]. In addition, this work showed that coordinating a larger ligand results in a higher proportion of the ordered component [151]. The results can be rationalized by the insights obtained from WE MD and EPR distance constraints (cf. above). That work showed that in the ligand-free state only one of α-helices is docked while the other is undocked [178]. Thus one can anticipate a faster component and a more ordered component in CW-EPR lineshapes of the unliganded protein. As ligand is added, both helices become docked and therefore increasing the more ordered component [178].

5 Concluding Remarks

Over the last few years various Cu(II) spin labels have shown great promise to enhance the power of EPR for the measurement of structure and dynamics of biomolecules. The protein label enormously reduces the width of the distance distribution thereby improving the fidelity of structural analysis [24, 207]. In addition, the spectral lineshapes at room temperature are highly sensitive to backbone dynamics [35]. Finally, the DNA label can measure distances that can be directly related to backbone conformations [123, 124]. Moreover, labeling to protein and nucleic acids is straightforward since it is performed in solution by the simple addition of a stoichiometric amount of Cu(II) to the label. The method, thus, does not require additional synthesis or purification. Thorough labeling protocols [221] and the effect of buffer choice on labeling efficiency [60] have also been reported for dHis. Methodology is also available to seamlessly model dHis based distance distributions and to combine structural constraints with coarse grained modeling [39, 126, 131, 197]. The recent development of combined EPR and enhanced sampling methodology to generate atomistic detailed transition pathways for slow seconds timescale conformational changes is likely to be impactful [165, 178]. Finally, in-cell structural studies using this label are on the horizon [222]. In this review, we have covered the vast strides in Cu(II) method development over the recent years that have drastically reduced data-collection times by utilizing deuteration, incorporating frequency-swept pulses, and employing strategic acquisition schemes to mitigate orientation selectivity effects. Moreover, orthogonal labeling schemes with Cu(II) gives access to measurements in the nanomolar regime [208]. The combination of these approaches has enhanced the ability of Cu(II) labels to report on important structural details and chemical equilibriums of functionally complex proteins and DNA.

Supplementary Information The online version contains supplementary material available at https://doi.org/10.1007/s00723-024-01658-8.

Author contributions JC: writing—original draft, writing—review and editing, visualizations, data collection. SP: data collection, writing—review and editing. SS: writing—review and editing, supervision.

Funding This work was financially supported by National Science Foundation [NSF BSF MCB-2006154].

Data availability Data is provided within the manuscript and is available on request.

Declarations

Conflict of interest The authors declare no competing interests.

Ethics approval This research did not contain any studies involving animal or human participants, nor did it take place in any private or protected area. No specific permissions were required for corresponding locations.

References

1. M.M. Roessler, E. Salvadori, Chem. Soc. Rev. **47**, 2534 (2018)
2. A. Kraft, Chem. Ind. Lond. **78**, 53 (2014)
3. P.C. Bruzzese, E. Salvadori, S. Jäger, M. Hartmann, B. Civalleri, A. Pöppl, M. Chiesa, Nat. Commun. **12**, 1–3 (2021)
4. R. Bikas, P. Aleshkevych, H. Hosseini-Monfared, J. Sanchiz, R. Szymczak, T. Lis, Dalt. Trans. **44**, 1782 (2015)
5. H.H. Haeri, V. Jerschabek, A. Sadeghi, D. Hinderberger, Macromol. Chem. Phys. **221**, 1 (2020)
6. S. Richert, J. Cremers, H.L. Anderson, C.R. Timmel, Chem. Sci. **7**, 6952 (2016)
7. J.P. Donoso, C.J. Magon, J.F. Lima, O.R. Nascimento, E. Benavente, M. Moreno, G. Gonzalez, J. Phys. Chem. C **117**, 24042 (2013)
8. F.D. Breitgoff, K. Keller, M. Qi, D. Klose, M. Yulikov, A. Godt, G. Jeschke, J. Magn. Reson. **308**, 106560 (2019)
9. C.G. Carson, K. Hardcastle, J. Schwartz, X. Liu, C. Hoffmann, R.A. Gerhardt, R. Tannenbaum, Eur. J. Inorg. Chem. **2009**, 2338 (2009)
10. M. Šimenas, M. Kobalz, M. Mendt, P. Eckold, H. Krautscheid, J. Banys, A. Pöppl, J. Phys. Chem. C **119**, 4898 (2015)
11. N. Marquardt, M. Dahlke, A. Schaate, ChemPlusChem **88**, 1 (2023)
12. A.M. Brugh, R. Wang, M.J. Therien, M.D.E. Forbes, ACS Omega **6**, 27865 (2021)
13. R. Wang, A.M. Brugh, J. Rawson, M.J. Therien, M.D.E. Forbes, J. Am. Chem. Soc. **139**, 9759 (2017)
14. G. Jeschke, Annu. Rev. Phys. Chem. **63**, 419 (2012)
15. M. Azarkh, V. Singh, O. Okle, I.T. Seemann, D.R. Dietrich, J.S. Hartig, M. Drescher, Nat. Protoc. **8**, 131 (2013)
16. O. Schiemann, T.F. Prisner, Q. Rev. Biophys. **40**, 1 (2007)
17. K.M. Schilling, L. Tao, B. Wu, J.T.M. Kiblen, N.C. Ubilla-Rodriguez, M.J. Pushie, R.D. Britt, G.P. Roseman, D.A. Harris, G.L. Millhauser, J. Mol. Biol. **432**, 4408 (2020)
18. L. Quintanar, G.L. Millhauser, *EPR of Copper Centers in the Prion Protein*, 1st edn. (Elsevier Inc., 2022)
19. D. Abdullin, N. Florin, G. Hagelueken, O. Schiemann, Angew. Chem. Int. Ed. **54**, 1827 (2015)
20. V. Kofman, O. Farver, I. Pecht, D. Goldfarb, J. Am. Chem. Soc. **118**, 1201 (1996)
21. Z. Yang, M.R. Kurpiewski, M. Ji, J.E. Townsend, P. Mehta, L. Jen-Jacobson, S. Saxena, Proc. Natl. Acad. Sci. U. S. A. **109**, 6366 (2012)
22. S.C. Drew, L.L. Su, C.L.L. Pham, D.J. Tew, C.L. Masters, L.A. Miles, R. Cappai, K.J. Barnham, J. Am. Chem. Soc. **130**, 7766 (2008)
23. B.K. Shin, S. Saxena, J. Phys. Chem. B **115**, 15067 (2011)
24. T.F. Cunningham, M.R. Putterman, A. Desai, W.S. Horne, S. Saxena, Angew. Chem. Int. Ed. **54**, 6330 (2015)
25. A. Collauto, S. von Bülow, D.B. Gophane, S. Saha, L.S. Stelzl, G. Hummer, S.T. Sigurdsson, T.F. Prisner, Angew. Chem. **132**, 23225 (2020)
26. W.L. Hubbell, H.S. Mchaourab, C. Altenbach, M.A. Lietzow, Structure **4**, 779 (1996)
27. M.J. Lawless, J.L. Sarver, S. Saxena, Angew. Chem. Int. Ed. **56**, 2115 (2017)
28. D.M. Engelhard, A. Meyer, A. Berndhäuser, O. Schiemann, G.H. Clever, Chem. Commun. **54**, 7455 (2018)

29. G.H. Clever, S.J. Reitmeier, T. Carell, O. Schiemann, Angew. Chem. Int. Ed. **49**, 4927 (2010)
30. L.C. Tabares, D.T. Daniel, J.L. Vázquez-Ibar, C. Kouklovsky, V. Alezra, S. Un, J. Phys. Chem. Lett. **14**, 3368 (2023)
31. G.E. Merz, P.P. Borbat, A.R. Muok, M. Srivastava, D.N. Bunck, J.H. Freed, B.R. Crane, J. Phys. Chem. B **122**, 9443 (2018)
32. A. Gamble Jarvi, A. Sargun, X. Bogetti, J. Wang, C. Achim, S. Saxena, J. Phys. Chem. B **124**, 7544 (2020)
33. T.F. Cunningham, M.D. Shannon, M.R. Putterman, R.J. Arachchige, I. Sengupta, M. Gao, C.P. Jaroniec, S. Saxena, J. Phys. Chem. B **119**, 2839 (2015)
34. A. Gamble Jarvi, X. Bogetti, K. Singewald, S. Ghosh, S. Saxena, Acc. Chem. Res. **54**, 1481 (2021)
35. K. Singewald, H. Hunter, T.F. Cunningham, S. Ruthstein, S. Saxena, Anal. Sens. **3**, 202200053 (2022)
36. M.J. Lawless, S. Ghosh, T.F. Cunningham, A. Shimshi, S. Saxena, Phys. Chem. Chem. Phys. **19**, 20959 (2017)
37. S. Ghosh, M.J. Lawless, G.S. Rule, S. Saxena, J. Magn. Reson. **286**, 163 (2018)
38. P.P. Borbat, J.H. Freed, in *Structural Information from Spin-Labels and Intrinsic Paramagnetic Centers in the Biosciences*, eds. by CR. Timmel, JR. Harmer. Pulse Dipolar Electron Spin Resonance: Distance Measurements (Springer Verlag, 2013), pp. 1–82
39. S. Ghosh, S. Saxena, G. Jeschke, Appl. Magn. Reson. **49**, 1281 (2018)
40. G.E. Fanucci, D.S. Cafiso, Curr. Opin. Struct. Biol. **16**, 644 (2006)
41. A.J. Fielding, M.G. Concilio, G. Heaven, M.A. Hollas, Molecules **19**, 16998 (2014)
42. W.L. Hubbell, C.J. López, C. Altenbach, Z. Yang, Curr. Opin. Struct. Biol. **23**, 725 (2013)
43. D. Goldfarb, Phys. Chem. Chem. Phys. **16**, 9685 (2014)
44. F. Wojciechowski, A. Groß, I.T. Holder, L. Knörr, M. Drescher, J.S. Hartig, Chem. Commun. **51**, 13850 (2015)
45. Z. Hasanbasri, K. Singewald, T.D. Gluth, B. Driesschaert, S. Saxena, J. Phys. Chem. B **125**, 5265 (2021)
46. N. Fleck, C.A. Heubach, T. Hett, F.R. Haege, P.P. Bawol, H. Baltruschat, O. Schiemann, Angew. Chemie Int. Ed. **59**, 9767 (2020)
47. G.Y. Shevelev, O.A. Krumkacheva, A.A. Lomzov, A.A. Kuzhelev, O.Y. Rogozhnikova, D.V. Trukhin, T.I. Troitskaya, V.M. Tormyshev, M.V. Fedin, D.V. Pyshnyi, E.G. Bagryanskaya, J. Am. Chem. Soc. **136**, 9874 (2014)
48. M. Qi, A. Groß, G. Jeschke, A. Godt, M. Drescher, J. Am. Chem. Soc. **136**, 15366 (2014)
49. A. Martorana, G. Bellapadrona, A. Feintuch, E. Di Gregorio, S. Aime, D. Goldfarb, J. Am. Chem. Soc. **136**, 13458 (2014)
50. J. Peisach, W.E. Blumberg, Arch. Biochem. Biophys. **165**, 691 (1974)
51. B.J. Hathaway, A.A.G. Tomlinson, Coord. Chem. Rev. **5**, 1 (1970)
52. I.M. Procter, B.J. Hathaway, P. Nicholls, J. Chem. Soc. A Inorganic Phys. Theor. 1678–1694 (1968). https://doi.org/10.1039/J19680001678
53. M. Valko, P. Pelikan, S. Biskupic, M. Mazur, Chem. Pap. **44**, 805 (1990)
54. A.H. Maki, B.R. McGarvey, J. Chem. Phys. **29**, 35 (1958)
55. D. Reinen, C. Friebel, Inorg. Chem. **23**, 791 (1984)
56. K.I. Silva, B.C. Michael, S.J. Geib, S. Saxena, J. Phys. Chem. B **118**, 8935 (2014)
57. S. Stoll, A. Schweiger, J. Magn. Reson. **178**, 42 (2006)
58. E.P. Wagner, K.C. Gronborg, S. Ghosh, S. Saxena, J. Chem. Educ. **96**, 1752 (2019)
59. K. Singewald, J.A. Wilkinson, Z. Hasanbasri, S. Saxena, Protein Sci. **31**, 1 (2022)
60. A. Gamble Jarvi, J. Casto, S. Saxena, J. Magn. Reson. **320**, 106848 (2020)
61. Y. Deligiannakis, M. Louloudi, N. Hadjiliadis, Coord. Chem. Rev. **1**, 1 (2000)
62. A.G. Maryasov, M.K. Bowman, J. Phys. Chem. B **108**, 9412 (2004)
63. T.F. Segawa, A. Doll, S. Pribitzer, G. Jeschke, J. Chem. Phys. **143**, 044201 (2015)
64. F. Jiang, J. McCracken, J. Peisach, J. Am. Chem. Soc. **112**, 9035 (1990)
65. J. McCracken, J. Peisach, D.M. Dooley, J. Am. Chem. Soc. **109**, 4064 (1987)
66. B.K. Shin, S. Saxena, Biochemistry **47**, 9117 (2008)
67. B.K. Shin, S. Saxena, J. Phys. Chem. A **115**, 9590 (2011)
68. D. Goldfarb, J.M. Fauth, Y. Tor, A. Shanzer, Y. Tor, A. Shanzer, J. Am. Chem. Soc. **113**, 1941 (1991)
69. J. Mccracken, J. Peisach, S. Pember, S.J. Benkovic, J.J. Villafranca, R.J. Miller, J. Am. Chem. Soc. **110**, 1069 (1988)

70. J. McCracken, P.R. Desai, N.J. Papadopoulos, J.J. Villafranca, J. Peisach, Biochemistry **27**, 4133 (1988)
71. W.B. Mims, J. Peisach, J. Chem. Phys. **69**, 4921 (1978)
72. D.J. Kosman, J. Peisach, W.B. Mims, Biochemistry **19**, 1304 (1980)
73. V. Singh, Z. Zhu, V.L. Davidson, J. McCracken, J. Am. Chem. Soc. **122**, 931 (2000)
74. J. McCracken, J. Peisach, C.E. Cote, M.A. McGuirl, D.M. Dooley, J. Am. Chem. Soc. **114**, 3715 (1992)
75. S. Jun, J.R. Gillespie, B.K. Shin, S. Saxena, Biochemistry **48**, 10724 (2009)
76. M. Ji, L. Tan, L. Jen-Jacobson, S. Saxena, Mol. Phys. **112**, 3173 (2014)
77. J.S. Hyde, J.J. Yin, W.K. Subczynski, T.G. Camenisch, J.J. Ratke, W. Froncisz, J. Phys. Chem. B **108**, 9524 (2004)
78. S. Saxena, J.H. Freed, J. Chem. Phys. **107**, 1317 (1997)
79. G. Jeschke, M. Pannier, A. Godt, H.W. Spiess, Chem. Phys. Lett. **331**, 243 (2000)
80. S. Milikisyants, F. Scarpelli, M.G. Finiguerra, M. Ubbink, M. Huber, J. Magn. Reson. **201**, 48 (2009)
81. A.D. Milov, A.B. Ponomarev, Y.D. Tsvetkov, Chem. Phys. Lett. **110**, 67 (1984)
82. M. Pannier, S. Veit, A. Godt, G. Jeschke, H.W. Spiess, J. Magn. Reson. **142**, 331 (2000)
83. T. Bahrenberg, S.M. Jahn, A. Feintuch, S. Stoll, D. Goldfarb, Magn. Reson. **2**, 161 (2021)
84. J.L. Du, G.R. Eaton, S.S. Eaton, Appl. Magn. Reson. **6**, 373 (1994)
85. A.J. Fielding, S. Fox, G.L. Millhauser, M. Chattopadhyay, P.M.H. Kroneck, G. Fritz, G.R. Eaton, S.S. Eaton, J. Magn. Reson. **179**, 92 (2006)
86. J. Casto, X. Bogetti, H.R. Hunter, Z. Hasanbasri, S. Saxena, J. Magn. Reson. **349**, 107413 (2023)
87. R. Owenius, G.R. Eaton, S.S. Eaton, J. Magn. Reson. **172**, 168 (2005)
88. P. Aggarwal, S.S. Eaton, G.R. Eaton, Appl. Magn. Reson. **47**, 1123 (2016)
89. J. Casto, A. Mandato, S. Saxena, J. Phys. Chem. Lett. **12**, 4681 (2021)
90. H. El Mkami, R. Ward, A. Bowman, T. Owen-Hughes, D.G. Norman, J. Magn. Reson. **248**, 36 (2014)
91. E.R. Canarie, S.M. Jahn, S. Stoll, J. Phys. Chem. Lett. **11**, 3396 (2020)
92. R. Ward, A. Bowman, E. Sozudogru, H. El-Mkami, T. Owen-Hughes, D.G. Norman, J. Magn. Reson. **207**, 164 (2010)
93. T. Schmidt, M.A. Wälti, J.L. Baber, E.J. Hustedt, G.M. Clore, Angew. Chem. Int. Ed. **55**, 15905 (2016)
94. S.M. Jahn, E.R. Canarie, S. Stoll, J. Phys. Chem. Lett. **13**, 5474 (2022)
95. J. Soetbeer, M. Hülsmann, A. Godt, Y. Polyhach, G. Jeschke, Phys. Chem. Chem. Phys. **20**, 1615 (2018)
96. A. Eggeling, J. Soetbeer, L. Fábregas-Ibáñez, D. Klose, G. Jeschke, Phys. Chem. Chem. Phys. **25**, 11145 (2023)
97. J. Soetbeer, M. Millen, K. Zouboulis, M. Hülsmann, A. Godt, Y. Polyhach, G. Jeschke, Phys. Chem. Chem. Phys. **23**, 5352 (2021)
98. M. Šimėnas, D. Klose, M. Ptak, K. Aidas, M. Mączka, J. Banys, A. Pöppl, G. Jeschke, Sci. Adv. **6**, 1 (2020)
99. D. Abdullin, O. Schiemann, ChemPlusChem **85**, 353 (2020)
100. O. Schiemann, C.A. Heubach, D. Abdullin, K. Ackermann, M. Azarkh, E.G. Bagryanskaya, M. Drescher, B. Endeward, J.H. Freed, L. Galazzo, D. Goldfarb, T. Hett, L. Esteban Hofer, L. Fábregas Ibáñez, E.J. Hustedt, S. Kucher, I. Kuprov, J.E. Lovett, A. Meyer, S. Ruthstein, S. Saxena, S. Stoll, C.R. Timmel, M. Di Valentin, H.S. McHaourab, T.F. Prisner, B.E. Bode, E. Bordignon, M. Bennati, G. Jeschke, J. Am. Chem. Soc. **143**, 17875 (2021)
101. B.E. Bode, D. Margraf, J. Plackmeyer, G. Dürner, T.F. Prisner, O. Schiemann, J. Am. Chem. Soc. **129**, 6736 (2007)
102. T. Schmidt, J.M. Louis, G.M. Clore, ChemBioChem **21**, 2998 (2020)
103. D. Abdullin, P. Brehm, N. Fleck, S. Spicher, S. Grimme, O. Schiemann, Chem. A Eur. J. **25**, 14388 (2019)
104. I. Kaminker, R. Barnes, S. Han, J. Magn. Reson. **279**, 81 (2017)
105. T. Kaufmann, T.J. Keller, J.M. Franck, R.P. Barnes, S.J. Glaser, J.M. Martinis, S. Han, J. Magn. Reson. **235**, 95 (2013)
106. A. Doll, S. Pribitzer, R. Tschaggelar, G. Jeschke, J. Magn. Reson. **230**, 27 (2013)
107. M. Tseitlin, R.W. Quine, G.A. Rinard, S.S. Eaton, G.R. Eaton, J. Magn. Reson. **213**, 119 (2011)
108. P.E. Spindler, S.J. Glaser, T.E. Skinner, T.F. Prisner, Angew. Chem. Int. Ed. **52**, 3425 (2013)

109. P.E. Spindler, I. Waclawska, B. Endeward, J. Plackmeyer, C. Ziegler, T.F. Prisner, J. Phys. Chem. Lett. **6**, 4331 (2015)
110. P.E. Spindler, P. Schöps, W. Kallies, S.J. Glaser, T.F. Prisner, J. Magn. Reson. **280**, 30 (2017)
111. A. Doll, G. Jeschke, J. Magn. Reson. **280**, 46 (2017)
112. A. Doll, G. Jeschke, J. Magn. Reson. **246**, 18 (2014)
113. T.W. Borneman, D.G. Cory, J. Magn. Reson. **225**, 120 (2012)
114. R. Tschaggelar, F.D. Breitgoff, O. Oberhänsli, M. Qi, A. Godt, G. Jeschke, Appl. Magn. Reson. **48**, 1273 (2017)
115. V. Denysenkov, P. van Os, T.F. Prisner, Appl. Magn. Reson. **48**, 1263 (2017)
116. Z. Hasanbasri, S. Saxena, Appl. Magn. Reson. **55**, 61–78 (2023)
117. R.G. Larsen, D.J. Singel, J. Chem. Phys. **98**, 5134 (1993)
118. B. Endeward, J.A. Butterwick, R. MacKinnon, T.F. Prisner, J. Am. Chem. Soc. **131**, 15246 (2009)
119. S. Stoller, G. Sicoli, T.Y. Baranova, M. Bennati, U. Diederichsen, Angew. Chem. Int. Ed. **50**, 9743 (2011)
120. M.R. Fleissner, M.D. Bridges, E.K. Brooks, D. Cascio, T. Kálai, K. Hideg, W.L. Hubbell, Proc. Natl. Acad. Sci. U. S. A. **108**, 16241 (2011)
121. N. Barhate, P. Cekan, A.P. Massey, S.T. Sigurdsson, Angew. Chem. Int. Ed. **46**, 2655 (2007)
122. N.R. Kamble, M. Gränz, T.F. Prisner, S.T. Sigurdsson, Chem. Commun. **52**, 14442 (2016)
123. S. Ghosh, M.J. Lawless, H.J. Brubaker, K. Singewald, M.R. Kurpiewski, L. Jen-Jacobson, S. Saxena, Nucleic Acids Res. **48**, 1 (2020)
124. S. Ghosh, J. Casto, X. Bogetti, C. Arora, J. Wang, S. Saxena, Phys. Chem. Chem. Phys. **22**, 26707 (2020)
125. R.T. McGibbon, K.A. Beauchamp, M.P. Harrigan, C. Klein, J.M. Swails, C.X. Hernández, C.R. Schwantes, L.P. Wang, T.J. Lane, V.S. Pande, Biophys. J. **109**, 1528 (2015)
126. X. Bogetti, S. Ghosh, A. Gamble Jarvi, J. Wang, S. Saxena, J. Phys. Chem. B **124**, 2788 (2020)
127. C.A. Heubach, Z. Hasanbasri, D. Abdullin, A. Reuter, B. Korzekwa, S. Saxena, O. Schiemann, Chem. A Eur. J. **29**, e202302541 (2023)
128. X. Bogetti, Z. Hasanbasri, H.R. Hunter, S. Saxena, Phys. Chem. Chem. Phys. **24**, 14727 (2022)
129. A. Gamble Jarvi, K. Ranguelova, S. Ghosh, R.T. Weber, S. Saxena, J. Phys. Chem. B **122**, 10669 (2018)
130. Z. Hasanbasri, N.A. Moriglioni, S. Saxena, Phys. Chem. Chem. Phys. **25**, 13275 (2023)
131. Z. Hasanbasri, M.H. Tessmer, S. Stoll, S. Saxena, Phys Chem Chem Phys. **26**(8), 6806–6816 (2024)
132. Z. Yang, J. Becker, S. Saxena, J. Magn. Reson. **188**, 337 (2007)
133. H. Ghimire, R.M. Mccarrick, D.E. Budil, G.A. Lorigan, Rep. Biochem. **48**, 5783 (2009)
134. T. Prisner, M. Rohrer, F. MacMillan, Annu. Rev. Phys. Chem. **52**, 279 (2001)
135. Y.D. Tsvetkov, A.D. Milov, A.G. Maryasov, Russ. Chem. Rev. **77**, 487 (2008)
136. A.W. Fischer, E. Bordignon, S. Bleicken, A.J. García-Sáez, G. Jeschke, J. Meiler, J. Struct. Biol. **195**, 62 (2016)
137. N. Alexander, A. Al-Mestarihi, M. Bortolus, H. Mchaourab, J. Meiler, Structure **16**, 181 (2008)
138. O. Dalmas, P. Sompornpisut, F. Bezanilla, E. Perozo, Nat. Commun. **5**, 1 (2014)
139. T. Hett, T. Zbik, S. Mukherjee, H. Matsuoka, W. Bönigk, D. Klose, C. Rouillon, N. Brenner, S. Peuker, R. Klement, H.J. Steinhoff, H. Grubmüller, R. Seifert, O. Schiemann, U.B. Kaupp, J. Am. Chem. Soc. **143**, 6981 (2021)
140. W.L. Hubbell, D.S. Cafiso, C. Altenbach, Nat. Struct. Biol. **7**, 735 (2000)
141. L. Galazzo, G. Meier, M. Hadi Timachi, C.A.J. Hutter, M.A. Seeger, E. Bordignon, Proc. Natl. Acad. Sci. U. S. A. **117**, 2441 (2020)
142. R. Dastvan, A. Rasouli, S. Dehghani-Ghahnaviyeh, S. Gies, E. Tajkhorshid, Nat. Commun. **13**, 1 (2022)
143. B. Joseph, A. Sikora, D.S. Cafiso, J. Am. Chem. Soc. **138**, 1844 (2016)
144. G.E. Fanucci, K.A. Coggshall, N. Cadieux, M. Kim, R.J. Kadner, D.S. Cafiso, Biochemistry **42**, 1391 (2003)
145. C. Altenbach, A.K. Kusnetzow, O.P. Ernst, K.P. Hofmann, W.L. Hubbell, Proc. Natl. Acad. Sci. U. S. A. **105**, 7439 (2008)
146. T. Schmidt, J. Jeon, W.M. Yau, C.D. Schwieters, R. Tycko, G.M. Clore, Proc. Natl. Acad. Sci. U. S. A. **119**, e2122308119 (2022)
147. D.P. Claxton, M. Quick, L. Shi, F.D. De Carvalho, H. Weinstein, J.A. Javitch, H.S. McHaourab, Nat. Struct. Mol. Biol. **17**, 822 (2010)

148. W.L. Hubbell, C. Altenbach, Curr. Opin. Struct. Biol. **4**, 566 (1994)
149. F. Torricella, A. Pierro, E. Mileo, V. Belle, A. Bonucci, Biochim. Biophys. Acta Proteins Proteomics **1869**, 140653 (2021)
150. J.M. Esquiaqui, E.M. Sherman, J.D. Ye, G.E. Fanucci, Biochemistry **55**, 4295 (2016)
151. K. Singewald, X. Bogetti, K. Sinha, G.S. Rule, S. Saxena, Angew. Chemie Int. Ed. **59**, 23040 (2020)
152. P.P. Borbat, A.J. Costa-Filho, K.A. Earle, J.K. Moscicki, J.H. Freed, Science **291**, 266 (2001)
153. S. Milikisiyants, S. Wang, R.A. Munro, M. Donohue, M.E. Ward, D. Bolton, L.S. Brown, T.I. Smirnova, V. Ladizhansky, A.I. Smirnov, J. Mol. Biol. **429**, 1903 (2017)
154. S.Y. Park, P.P. Borbat, G. Gonzalez-Bonet, J. Bhatnagar, A.M. Pollard, J.H. Freed, A.M. Bilwes, B.R. Crane, Nat. Struct. Mol. Biol. **13**, 400 (2006)
155. D.A. Nyenhuis, T.D. Nilaweera, J.K. Niblo, N.Q. Nguyen, K.H. Dubay, D.S. Cafiso, J. Am. Chem. Soc. **142**, 10715 (2020)
156. L.G. Cuello, D.M. Cortes, E. Perozo, Science (80-.). **306**, 491 (2004)
157. V. Singh, M. Azarkh, T.E. Exner, J.S. Hartig, M. Drescher, Angew. Chem. Int. Ed. **48**, 9728 (2009)
158. B.J. Gaffney, M.D. Bradshaw, S.D. Frausto, F. Wu, J.H. Freed, P. Borbat, Biophys. J. **103**, 2134 (2012)
159. D.M. Yin, J.S. Hannam, A. Schmitz, O. Schiemann, G. Hagelueken, M. Famulok, Angew. Chem. Int. Ed. **56**, 8417 (2017)
160. Z. Yang, M.R. Kurpiewski, M. Ji, J.E. Townsend, P. Mehta, L. Jen-Jacobson, S. Saxena, Proc. Natl. Acad. Sci. U. S. A. **109**, 3 (2012)
161. H. Celia, N. Noinaj, S.D. Zakharov, E. Bordignon, I. Botos, M. Santamaria, T.J. Barnard, W.A. Cramer, R. Lloubes, S.K. Buchanan, Nature **538**, 60 (2016)
162. C. Pliotas, R. Ward, E. Branigan, A. Rasmussen, G. Hagelueken, H. Huang, S.S. Black, I.R. Booth, O. Schiemann, J.H. Naismith, Proc. Natl. Acad. Sci. U. S. A. **109**, E2675 (2012)
163. G. Hagelueken, J. Hoffmann, E. Schubert, F.G. Duthie, N. Florin, L. Konrad, D. Imhof, E. Behrmann, N. Morgner, O. Schiemann, Biophys. J. **110**, 2642 (2016)
164. I. Vercellino, L. Rezabkova, V. Olieric, Y. Polyhach, T. Weinert, R.A. Kammerer, G. Jeschke, V.M. Korkhov, Proc. Natl. Acad. Sci. U. S. A. **114**, E9821 (2017)
165. X. Bogetti, S. Saxena, Chempluschem **89**(1), e202300506 (2023)
166. B. Roux, S.M. Islam, J. Phys. Chem. B **117**, 4733 (2013)
167. S.J. Hirst, N. Alexander, H.S. Mchaourab, J. Meiler, J. Struct. Biol. **173**, 506 (2011)
168. M.H. Tessmer, S. Stoll, PLoS Comput. Biol. **19**, 1 (2023)
169. D. del Alamo, L. DeSousa, R.M. Nair, S. Rahman, J. Meiler, H.S. McHaourab, Proc. Natl. Acad. Sci. U. S. A. **119**, 1 (2022)
170. G. Jeschke, Protein Sci. **27**, 76 (2018)
171. M.H. Tessmer, E.R. Canarie, S. Stoll, Biophys. J. **121**, 3508 (2022)
172. M. Teucher, H. Zhang, V. Bader, K.F. Winklhofer, A.J. García-Sáez, A. Rajca, S. Bleicken, E. Bordignon, Sci. Rep. **9**, 1 (2019)
173. S.L. Meichsner, Y. Kutin, M. Kasanmascheff, Angew. Chem. Int. Ed. **60**, 19155 (2021)
174. N. Fleck, C. Heubach, T. Hett, S. Spicher, S. Grimme, O. Schiemann, Chem. A Eur. J. **27**, 5292 (2021)
175. B. Joseph, V.M. Tormyshev, O.Y. Rogozhnikova, D. Akhmetzyanov, E.G. Bagryanskaya, T.F. Prisner, Angew. Chem. Int. Ed. **55**, 11538 (2016)
176. R.N. Armstrong, Chem. Res. Toxicol. **10**, 2 (1997)
177. Y. Zhan, G.S. Rule, Biochemistry **43**, 7244 (2004)
178. X. Bogetti, A. Bogetti, J. Casto, G. Rule, L. Chong, S. Saxena, Protein Sci. **32**, e4770 (2023)
179. E. Grahn, M. Novotny, E. Jakobsson, A. Gustafsson, L. Grehn, B. Olin, D. Madsen, M. Wahlberg, B. Mannervik, G.J. Kleywegt, Acta Crystallogr. Sect. D Biol. Crystallogr. **62**, 197 (2006)
180. G.A. Huber, S. Kim, Biophys. J. **70**, 97 (1996)
181. D.M. Zuckerman, L.T. Chong, Annu. Rev. Biophys. **46**, 43 (2017)
182. J.D. Russo, S. Zhang, J.M.G. Leung, A.T. Bogetti, J.P. Thompson, A.J. Degrave, P.A. Torrillo, A.J. Pratt, K.F. Wong, J. Xia, J. Copperman, J.L. Adelman, M.C. Zwier, D.N. Lebard, D.M. Zuckerman, L.T. Chong, J. Chem. Theory Comput. **18**, 638 (2022)

183. I. Le Trong, R.E. Stenkamp, C. Ibarra, W.M. Atkins, E.T. Adman, Proteins Struct. Funct. Genet. **48**, 618 (2002)
184. F.W. Outten, C.E. Outten, J. Hale, T.V. O'Halloran, J. Biol. Chem. **275**, 31024 (2000)
185. J. Casto, A. Mandato, L. Hofmann, I. Yakobov, S. Ghosh, S. Ruthstein, S. Saxena, Chem. Sci. **13**, 1693 (2022)
186. A.M. Fleming, C.J. Burrows, Chem. Soc. Rev. **49**, 6524 (2020)
187. K. Yamamoto, A. Ishihama, Mol. Microbiol. **56**, 215 (2005)
188. K.S. Chaturvedi, J.P. Henderson, Front. Cell. Infect. Microbiol. **5**, 3 (2014)
189. D.J. Martell, C.P. Joshi, A. Gaballa, A.G. Santiago, T.Y. Chen, W. Jung, J.D. Helmann, P. Chen, Proc. Natl. Acad. Sci. U. S. A. **112**, 13467 (2015)
190. S.J. Philips, M. Canalizo-Hernandez, I. Yildirim, G.C. Schatz, A. Mondragón, T.V. O'Halloran, Science (80-.). **349**, 877 (2015)
191. H. Sameach, A. Narunsky, S. Azoulay-Ginsburg, L. Gevorkyan-Aiapetov, Y. Zehavi, Y. Moskovitz, T. Juven-Gershon, N. Ben-Tal, S. Ruthstein, Structure **25**, 988 (2017)
192. L. Hofmann, A. Mandato, S. Saxena, S. Ruthstein, Biophys. Rev. **14**, 1141 (2022)
193. I. Yakobov, A. Mandato, L. Hofmann, K. Singewald, Y. Shenberger, L. Gevorkyan-Airapetov, S. Saxena, S. Ruthstein, Protein Sci. **31**, e4309 (2022)
194. C. Fang, S.J. Philips, X. Wu, K. Chen, J. Shi, L. Shen, J. Xu, Y. Feng, T.V. O'Halloran, Y. Zhang, Nat. Chem. Biol. **17**, 57 (2021)
195. W. Shi, B. Zhang, Y. Jiang, C. Liu, W. Zhou, M. Chen, Y. Yang, Y. Hu, B. Liu, IScience **24**, 102449 (2021)
196. C.P. Joshi, D. Panda, D.J. Martell, N.M. Andoy, T.-Y. Chen, A. Gaballa, J.D. Helmann, P. Chen, Proc. Natl. Acad. Sci. **109**, 15121 (2012)
197. H. Sameach, S. Ghosh, L. Gevorkyan-Airapetov, S. Saxena, S. Ruthstein, Angew. Chem. Int. Ed. **58**, 3053 (2019)
198. G.R. Cornelis, Nat. Rev. Microbiol. **4**, 811 (2006)
199. G.R. Cornelis, Nat. Rev. Mol. Cell Biol. **3**, 742 (2002)
200. G. Prehna, M.I. Ivanov, J.B. Bliska, C.E. Stebbins, Cell **126**, 869 (2006)
201. W.L. Lee, J.M. Grimes, R.C. Robinson, Nat. Struct. Mol. Biol. **22**, 248 (2015)
202. M.F. Peter, A.T. Tuukkanen, C.A. Heubach, A. Selsam, F.G. Duthie, D.I. Svergun, O. Schiemann, G. Hagelueken, Structure **27**, 1416 (2019)
203. M. Oranges, J.L. Wort, M. Fukushima, E. Fusco, K. Ackermann, B.E. Bode, J. Phys. Chem. Lett. **13**, 7847 (2022)
204. J.L. Wort, S. Arya, K. Ackermann, A.J. Stewart, B.E. Bode, J. Phys. Chem. Lett. **12**, 2815 (2021)
205. J.L. Wort, K. Ackermann, A. Giannoulis, A.J. Stewart, D.G. Norman, B.E. Bode, Angew. Chem. Int. Ed. **58**, 11681 (2019)
206. Z. Hasanbasri, M. Poncelet, H. Hunter, B. Driesschaert, S. Saxena, J. Magn. Reson. **347**, 107363 (2023)
207. V. Vitali, K. Ackermann, G. Hagelueken, B.E. Bode, Appl. Magn. Reson. **55**, 187 (2023)
208. K. Ackermann, C.A. Heubach, O. Schiemann, B.E. Bode, J. Phys. Chem. Lett. **15**, 1455 (2024)
209. A. Mandato, Z. Hasanbasri, S. Saxena, J. Phys. Chem. Lett. **14**, 8909 (2023)
210. J.L. Wort, K. Ackermann, A. Giannoulis, A.J. Stewart, D.G. Norman, B.E. Bode, Angew. Chem. **131**, 11807 (2019)
211. G.J. Pielak, C. Li, A.C. Miklos, A.P. Schlesinger, K.M. Slade, G.F. Wang, I.G. Zigoneanu, Biochemistry **48**, 9170 (2009)
212. A. Gamble Jarvi, T.F. Cunningham, S. Saxena, Phys. Chem. Chem. Phys. **21**, 10238 (2019)
213. P.R. Steed, R.A. Stein, S. Mishra, M.C. Goodman, H.S. McHaourab, Biochemistry **52**, 5790 (2013)
214. O. Schiemann, P. Cekan, D. Margraf, T.F. Prisner, S.T. Sigurdsson, Angew. Chem. Int. Ed. **48**, 3292 (2009)
215. J.E. Lovett, A.M. Bowen, C.R. Timmel, M.W. Jones, J.R. Dilworth, D. Caprotti, S.G. Bell, L.L. Wong, J. Harmer, Phys. Chem. Chem. Phys. **11**, 6840 (2009)
216. Z. Yang, D. Kise, S. Saxena, J. Phys. Chem. B **114**, 6165 (2010)
217. A.M. Bowen, M.W. Jones, J.E. Lovett, T.G. Gaule, M.J. McPherson, J.R. Dilworth, C.R. Timmel, J.R. Harmer, Phys. Chem. Chem. Phys. **18**, 5981 (2016)

218. D.M. Freed, A.K. Khan, P.S. Horanyi, D.S. Cafiso, Biochemistry **50**, 8792 (2011)
219. T.F. Cunningham, S. Pornsuwan, W.S. Horne, S. Saxena, Protein Sci. **25**, 1049 (2016)
220. T.F. Cunningham, M.S. McGoff, I. Sengupta, C.P. Jaroniec, W.S. Horne, S. Saxena, Biochemistry **51**, 6350 (2012)
221. K. Singewald, J.A. Wilkinson, S. Saxena, Bio-Protocol **11**(24), e4258 (2021)
222. Y. Shenberger, L. Gevorkyan-Airapetov, M. Hirsch, L. Hofmann, S. Ruthstein, Chem. Commun. **59**, 10524 (2023)

Authors and Affiliations

Joshua Casto[1] · Shramana Palit[1] · Sunil Saxena[1]

✉ Sunil Saxena
sksaxena@pitt.edu

Joshua Casto
jac246@pitt.edu

Shramana Palit
shp176@pitt.edu

[1] Department of Chemistry, University of Pittsburgh, Pittsburgh, PA 15260, USA